CRITICAL CURRENT ENHANCEMENT IN MAGNETIC SPIN-TRANSFER NANO-DEVICES THROUGH DOPING WITH THE RARE EARTH TERBIUM

A Dissertation

Presented to the Faculty of the Graduate School

of Cornell University

in Partial Fulfillment of the Requirements for the Degree of

Doctor of Philosophy

by

Eric Michael Ryan

August 20 2012

CRITICAL CURRENT ENHANCEMENT IN MAGNETIC SPIN-TRANSFER NANO-DEVICES THROUGH DOPING WITH THE RARE EARTH TERBIUM

Eric Michael Ryan, Ph.D.

Cornell University 2012

In this thesis, we fabricate magnetic nanopillars and dramatically enhance their damping through terbium doping in order to suppress the various spin-transfer effects, to the potential benefit of magnetic hard drive read head technology. This enhancement is much stronger at lower temperatures, and we can understand the 1/T temperature dependence observed through the application of established theory from the iron garnets. We also show that terbium doping can address technological problems with hard drive read heads. In particular, by inhibiting the microwave noise until a higher turn-on current is reached, without compromising the ability of the device to switch with reasonable power in times scales as short as 1 nsec, terbium-doped structures point the way forward for future designs. Finally, we make direct FMR measurements of the Gilbert phenomenological damping parameter at the center of these effects, and these measurements also suggest cobalt-iron alloys as systems for potential follow-up work.

BIOGRAPHICAL SKETCH

Eric Ryan was born in California, and with the exception of a four year stint in Pennsylvania mainly concerning shoe-tying and addition, remained there through his graduation from Foothill High School. He then sought education in Texas, attending Rice University and graduating with majors in Electrical Engineering and Chemical Physics. He studied mesoscopic systems and single electron tunneling under Alex Rimberg for his senior thesis.

This brought him to Cornell, where he joined the Buhrman group, a basement-dwelling organization for converting Louie's Lunch into data, and dedicated to answering the I.C.P.'s challenge to uncover the inner workings of magnets. Here he labored many years working to make ever smaller samples and larger signals.

Early in his graduate career, Thalia Mills lured Eric out of the basement to the physics students' reoccurring Ultimate Frisbee game. Here he learned the truth that dogs have long known: running is no chore when pursuing a rotating disk. This interest would grow into the second best way to raise his heart rate, the first being odd noises coming from the pumps in Clark Hall.

Allie King, fellow Rice graduate and science enthusiast, also came to Ithaca for graduate study. Allie won the race to a Cornell dissertation by a full year with her treatise on surface water flowing through vegetation. They plan to combine their talents and open a clinic extolling the virtues of magnetic water for your health,[1] as Drs. Ryan and King. They were married on campus in 2007 on the shores of Houston Pond.

A long period of study and struggle produced this document. It should be noted that two hard drives failed during the production of this thesis. The au-

[1] No, not really.

thor recognizes the irony in this, but does not appreciate it. He plans to continue his study of the practical aspects of spin-transfer with the S.T.T. corporation, founded by Andy Kent, in Ithaca and elsewhere.

I had been in the wilderness and gone through adversity.

-Richard Nixon, on his wilderness years

The arena is empty except for one man,
Still driving and striving as fast as he can.
The sun has gone down and the moon has come up,
And long ago somebody left with the cup,
But he’s driving and striving and hugging the turns,
And thinking of someone for whom he still burns.

He’s going the distance.

-Cake, "The Distance"

ACKNOWLEDGEMENTS

First and foremost I would like to acknowledge my special committee for reading and improving this work on an abbreviated schedule: Bruce van Dover, Paul McEuen, and especially my advisor Robert Buhrman, who provided many years of advice and direction. I also thank Piet Brouwer, who was always available when I needed to improve my theoretical understanding of some topic, especially during my A-exam. I gratefully acknowledge the National Science Foundation, the Office of Naval Research, and the Department of Education GAANN Fellowship program for their financial support of my studies at Cornell.

Since it is permissible to philosophize during forward material of a dissertation, allow me a moment to discuss a grammatical choice. The word I does not appear[2] in the body of this thesis, only we. This is not an oversight. Every piece of equipment I used was shared, every technique built upon previous ones, every idea I had was discussed with others. Every publication cites previous work, and its quality is judged by how often it is in turn cited by others. Our system of assigning credit to the first to publish has its flaws, but it reflects an important truth: it isn't science until it is shared with the world. The mad man toiling alone in the basement, waiting for lightning to strike to create his monster, exists only in fiction. Science is a product of and for society.

In this spirit I would like to mention the many members of the Buhrman and Ralph groups, past and present, who have contributed not only to this work but to my development as a scientist: Ozhan Ozatay, especially for his help with low temperature work, Pat Braganca, especially for his assistance with the pulse work, Nathan Emley and Jordan Katine, for patterning some of the samples

[2]Except, of course, to denote current.

while Cornell's e-beam writer was down, Andrei Garcia for his help with low temperature work, Praveen Gowtham and Takahiro Moriyama, for their help with the FMR measurements, Greg Fuchs, for the ST-FMR work, Jack Sankey and Kiran Thadani, for their help with the high frequency set-up, Eileen Tan, John Read, and Jon Shu for their help with the XPS measurements necessary to calibrate the Terbium doping, Ilya Krivorotov, Phil Mather, Andrew Perrella, Preeti Chalsani, Janis Chang, Vlad Pribiag, Hsinwei Tseng, Yun Li, Oukjae Lee, Luqiao Liu, Junbo Park, and Chi-Feng Pai. I have benefited greatly from many useful and involved conversations with all of you, and could not have come this far without your help in many forms.

I would also like to thank the CNF staff, as well as Clark staff members Jon Shu and Eric Smith, for being far more helpful than their positions might require, and the members of the Γ.A. Scientific Society, for providing a nourishing and stimulating environment. And of course, I must thank my parents, Ann and Dennis Ryan, whose proof-reading of this document (despite not always believing it was written in English) represents only the latest of innumerable sacrifices over these many years in the interest of my education and development.

Finally, I am eternally grateful to my wife, Allie, who supported me when my hour of need turned out to be long indeed.

TABLE OF CONTENTS

LIST OF TABLES

LIST OF FIGURES

CHAPTER 1

INTRODUCTION

This thesis is concerned with a series of experiments on the effects of increasing the damping in a spin-transfer system, using the rare earth terbium as means. Chapter 2 discusses the importance this work could have for hard drive read heads and provides the theoretical context to understand the work. Chapter 3 highlights the experimental techniques necessary to create the nanostructures and measure them. Chapter 4 involves the DC switching results and subsequently their temperature dependence, with good correspondence to theory. Finally, with an eye toward applications, chapter 5 examines three topics: the microwave noise that constitute the chief problem for hard drive read heads, pulsed switching measurements at speeds comparable to industrial demands (to insure that the higher damping devices are compatible), and direct measurements of the damping parameter that underlies all the research.

CHAPTER 2

MOTIVATION AND THEORY

2.1 Motivation

The introduction of Giant Magneto-Resistance (GMR) read-heads in the 1990s enabled hard drive densities, which had been lagging Moore's Law, to increase at a rate even faster than that of processor power. It is because of this transition that hard drive space is no longer at a premium. The bottleneck in achieving higher densities in hard drives has often been the signal-to-noise ratio (SNR) in the read head. Poor sensitivity in the read head requires larger bit sizes to produce more signal in order to insure reliability. With a pick-up coil, the signal is proportional to, among other things, the area of the coil, so it decreases at smaller sizes. In a GMR CPP device, the signal is proportional to the resistance, and therefore inversely proportional to the cross-sectional area of the device, and thus the signal increases at smaller device sizes. Below a certain size scale, the GMR device will be superior to the coil. However, should the cross-sectional area of the device become too small, then the density of the current passing though it will approach that required for spin-transfer effects and greatly change the nature of the device.

The spin-transfer effect is the complement to GMR. A sufficiently powerful spin current can reverse the orientation of a magnetic layer. At high sense currents, spin-transfer will pin the read head into the orientation favored by the current, rather than leaving it sensitive to the field that it is flying over. Even lower currents can excite microwave noise that impairs device performance.

Our earlier work[1] addressed this concern with a modified design. By replacing the fixed layer with a Synthetic AntiFerromagnet (SAF), in this case two cobalt layers antiferromagnetically coupled with Ru to have opposite orientation, two effects were achieved. First, the dipole field on the free layer was reduced, as the thickness of the two cobalt layers was chosen so that their fields would cancel at the free layer. Second, the critical currents increased because the opposing cobalt layers reduced the polarization of the spin current injected into the spacer layer. While this would be beneficial for hard drive applications, the reduced polarization also reduces the GMR signal that the hard drive read head relies on. Both the parasitic spin-transfer effect and the beneficial GMR effect stem from spin polarization, so altering the polarization will not distinguish between the effects. What is needed is a way to impair the dynamic process of spin-transfer without affecting the static process of GMR. The answer to this quandary is the enhanced damping that terbium doping can provide.

From the standpoint of scientific curiosity, consider the role that damping plays in spin-transfer. It is believed, for solid theoretical reasons, that the spin-transfer critical currents are directly proportional to the damping, as damping directly opposes the spin-transfer torque. However, no one has directly varied the intrinsic damping in a spin-transfer system before, so the work reported here represents the first investigation of this dependence in these systems.

2.2 Giant Magneto-Resistance

Consider a wire with two magnetic (e.g., cobalt) elements, separated and surrounded by non-magnetic spacer material (e.g., copper). In ferromagnets, scat-

tering probabilities (conductivities) are spin dependent. As electrons pass from a Cu layer into a Co layer, those whose spin direction is opposite the local moment of the Co layer will be more likely to scatter off the interface and away from the Co layer. Even those electrons with unfavorable spins that are transmitted will undergo a spatial precession, and within a few monolayers any component of spin transverse to the magnetization will be gone.[2] We can thus picture the ferromagnetic components of our wire as acting as spin filters, using scattering to align the spin of electrons passing through them.

A more precise quantitative description requires consideration of how the spin-dependent band structures interact at the Fermi surface. The results of such a calculation, done by Stiles[3] for the Co-Cu system, are shown in Figure 2.1. The spin-dependent scattering is clearly evident in the difference between the majority and minority states.

This filtering effect leaves the current passing through the Co layer with a spin polarization, which it maintains, upon exiting the Co layer back into the Cu layer, until some other scattering event (for example phonon interactions) destroys the polarization. Thus, if the second Co layer is close enough to the first Co layer that such scattering events are unlikely (that is, if the spacer layer is small compared to the mean free path), then there will be a spin-polarized current incident on the second Co layer. This scenario is the basis of two important effects relating to this research: Giant Magneto-Resistance (GMR) and the Spin-Transfer (ST) effect.

In an idealized system where the filtering is complete, only electrons with spin aligned to the first layer will pass through the spacer layer and be incident on the second layer. Thus, no current will flow in the anti-parallel case,

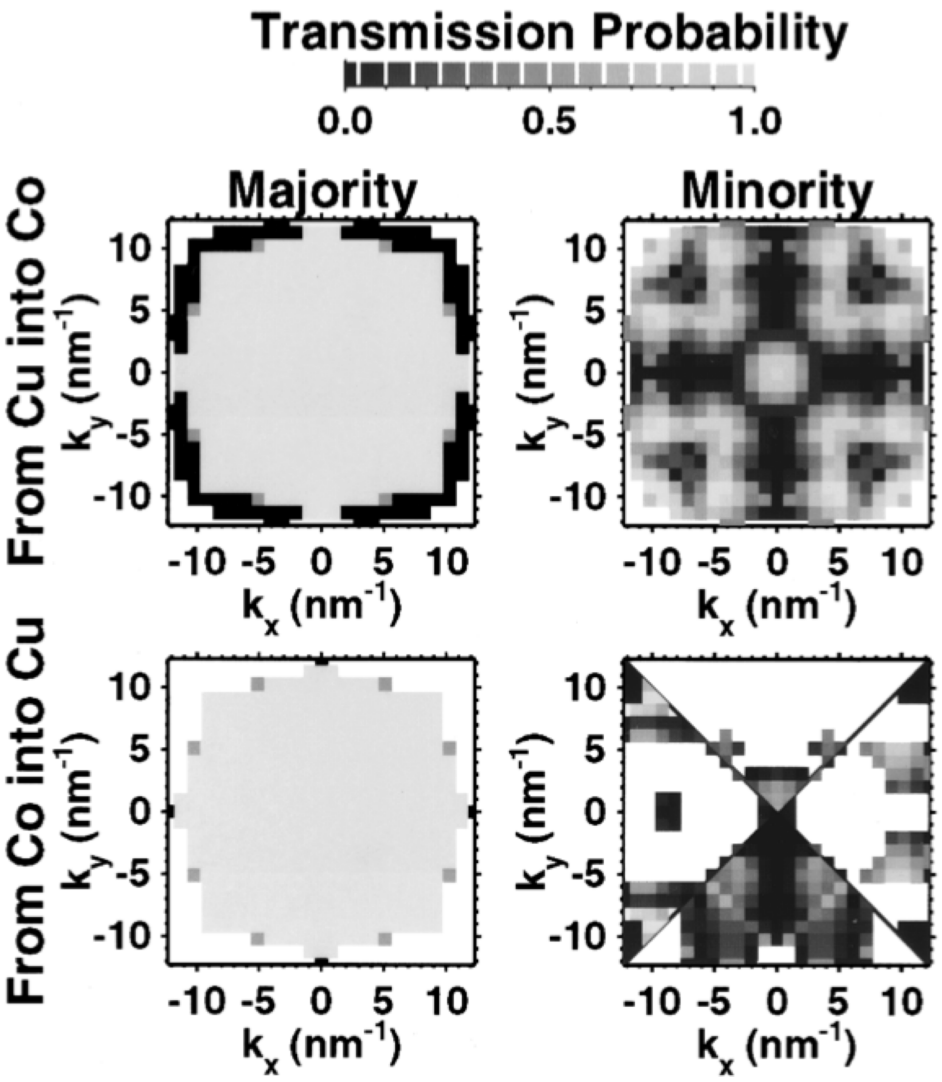

Figure 2.1: Spin-dependent transmission probabilities for Cu/Co (001), from first-principles calculation of the band structure at the Fermi surface. From Stiles.[3]

when the magnetic direction of the second layer is in the opposite direction from the first layer, while half of the electrons will pass through in the parallel case. This large difference in conductivity arising from a change in magnetic orientation forms the basis of GMR. In a less idealized system the polarization will be some fraction p and current will flow even in the anti-parallel case, but with more scattering and resistance than in the parallel case. Consider Figure

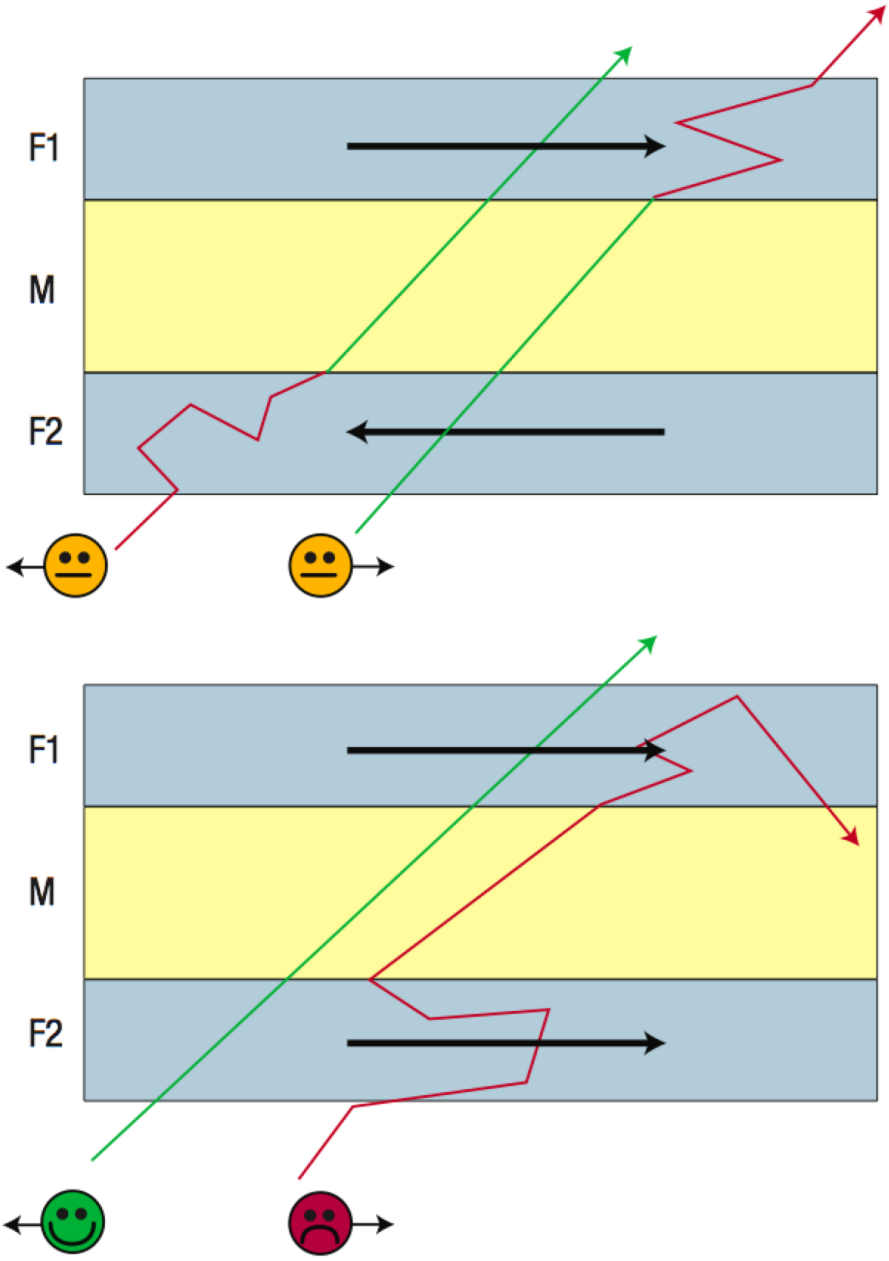

Figure 2.2: Two Channel Model. When the magnetic layers are antiparallel (above) electrons of any spin orientation are scattered. When the magnetic layers are parallel (below) then one orientation will experience very little scattering, and act as a short, carrying most of the current and producing a lower resistance than the antiparallel case. Note that this diagram is for the original Fe/Cr/Fe system and shows minority carriers preferentially transmitted, reversed from the modern systems with, for example, copper spacers. From Chappert.[4]

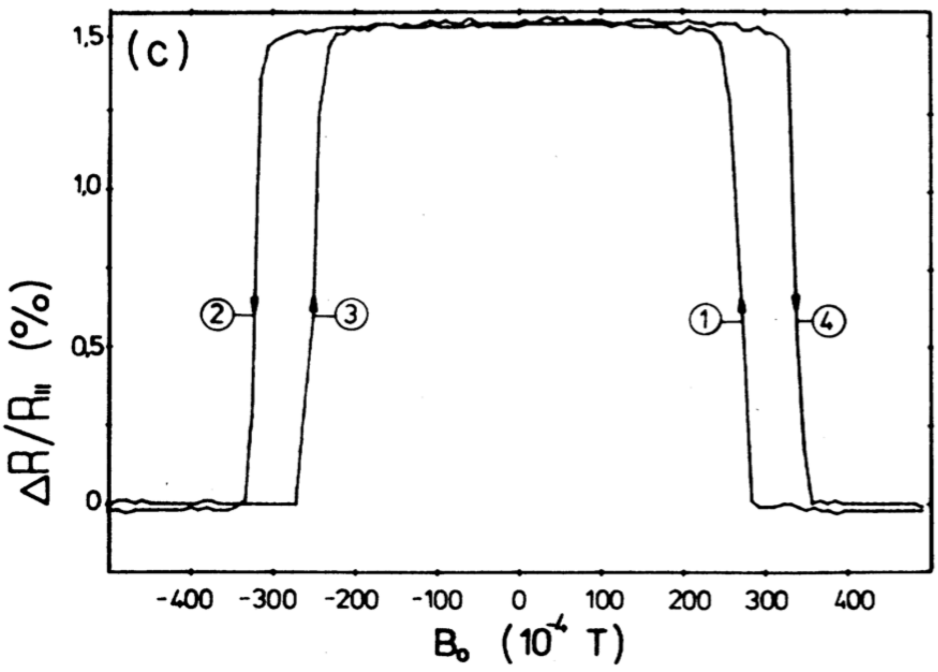

Figure 2.3: The first observations of GMR. The Fe-Cr-Fe trilayer is anti-ferromagnetically coupled, so the antiparallel state is stable at zero field. From Binasch.[5]

2.2. When the magnetic layers are antiparallel electrons of any spin orientation are scattered. When the magnetic layers are parallel, then one orientation will experience very little scattering and act as a short, carrying most of the current and producing a lower resistance than the antiparallel case. The strength of this effect is measured by ΔR, the difference in resistance between the two states divided by the smaller resistance.

GMR was first demonstrated by Binasch et al.[5] in the Fe-Cr-Fe system in 1988 and later confirmed with more layers for a larger signal by Baibich et al.[6]. These groups shared the Nobel Prize in 2007 for their discovery. The first observations, using a simple trilayer system, are shown in Figure 2.3. In zero field, the two Fe layers are anti-parallel and the high resistance state is measured. When the field is large, both Fe layers align with the field and the parallel, low

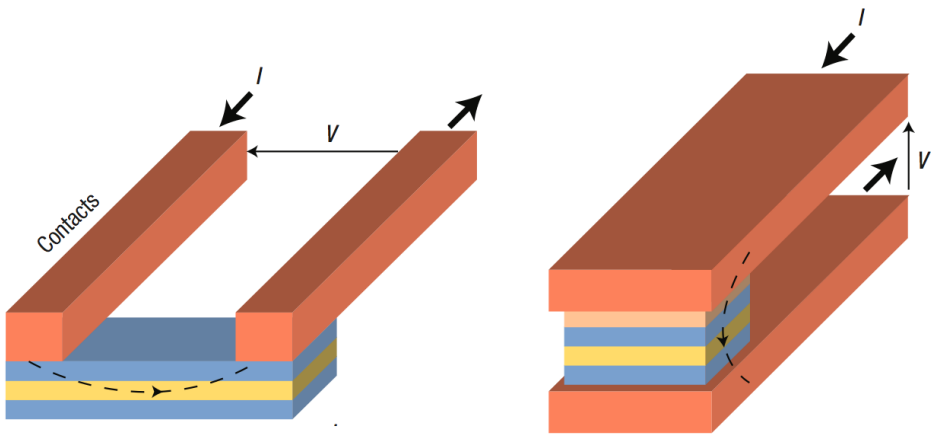

Figure 2.4: Spin Valves. On the left is the Current In Plane (CIP) design, where scattering can cause electrons to cross the interfaces many times or not at all. On the right is the Current Perpendicular to Plane (CPP) design used in this thesis, where electrons cross each interface once. The blue layers are magnetic. From Chappert.[4]

resistance state is measured. Thus the magnetic states of the system can be distinguished with an electrical measurement.

These first experiments used the Current-In-Plane (CIP) design, but in this work, as in most spin-transfer experiments, we use the Current-Perpendicular-to-Plane (CPP) geometry, first realized for GMR at Michigan State in 1991[7]. Figure 2.4 elucidates the differences. The CIP design is easier to fabricate, but the CPP design is simpler to analyze theoretically, as the path of the current is unambiguous. In order to achieve high enough resistance to measure the three-layer CPP structure, the dimensions are made small so that the resistance, and thus ΔR, is larger.

GMR stacks are used as magnetic field sensors, for example, in the read head of a hard drive. Typically one layer is made magnetically hard, or resistant to changing its magnetization, and is termed the "fixed layer," as opposed to

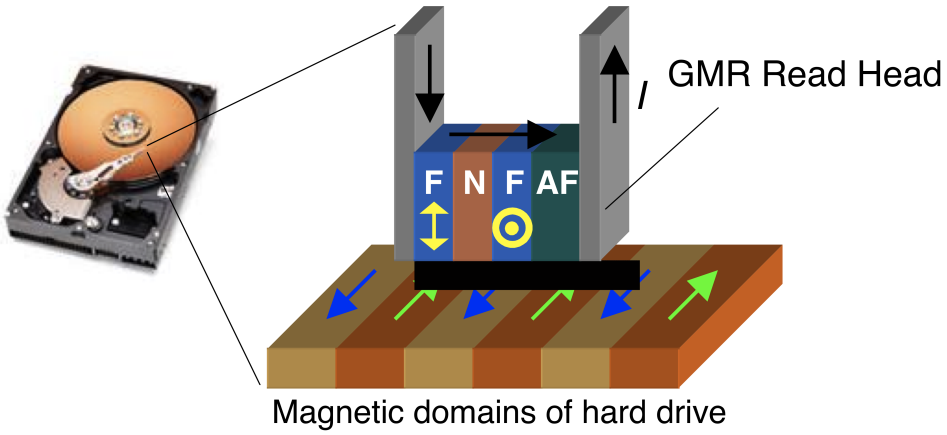

Figure 2.5: Hard Drive Read Head. The free layer changes direction in response to the bits stored on the drive. When the sense current I has a large density, spin-transfer effects hamper performance.

the magnetically soft "free layer." Permalloy (Py) is an alloy of iron and nickel ($Ni_{81}Fe_{19}$) that is magnetically soft with very low magnetostriction, and commonly used by industry for this purpose. The magnetic hardening can be done in a number of ways, such as making the fixed layer thick, changing the shape, changing the material composition, or 'pinning' — coupling the fixed layer to an anti-ferromagnet or forming an SAF. Often several of these methods are used in combination. If the fixed layer is insensitive to external fields while the free layer follows them easily, then the GMR stack will sense the direction of any nearby field by being in the low resistance parallel state when the nearby field matches the direction of the fixed layer, and in the high resistance anti-parallel state when the nearby field is in the opposite direction (see Figure 2.5). In the case of the hard-drive read head, this nearby field is the bit stored on the hard drive medium. Passing a current through the GMR stack creates a voltage, which the electronic system can manipulate, that is high or low depending on the magnetic state (1 or 0) stored on the drive. However, as industry makes the lateral dimensions of the GMR sensors smaller, both for spatial resolution and

to increase the signal by increasing the resistance, the current density creating the read voltage grows larger. Large current densities will hamper hard drive performance by entering the regime of the spin-transfer effect, discussed in the next section.

2.3 Spin-Transfer Effect

The spin-transfer effect is the complement to GMR. Instead of considering the effect of the magnetic orientation on the current, we consider the effect of the current on the magnetic orientation. The spin-filtering effect discussed above causes the net spin, and thus the angular momentum, of the current to change, and this change in angular momentum of the current must be matched with an opposite change in the magnet's angular momentum, in accordance with Newton's Third Law. This change is manifested as a torque (the spin-transfer torque) that changes the direction of the magnetization (see Figure 2.6). This effect implies that a sufficiently powerful spin current could change the orientation of the magnetic layer it passes through, and may even flip the direction of the magnetization entirely. As electrons polarized from the fixed layer interact with the free layer, their spin component transverse to the free layer's magnetization is absorbed by the free layer, moving it into alignment with the fixed layer. This "transfer" of spin from the fixed to the free layer gives the effect its name.

If the electrons are flowing from the fixed layer to the free layer, then the parallel orientation is stable, and the spin torque will move the two layers into alignment. If current flows in the opposite direction, one could imagine the effects discussed above creating a spin torque on the fixed layer. This does in-

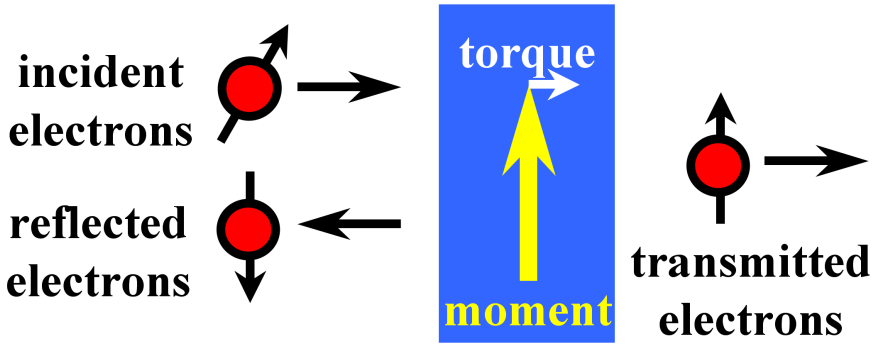

Figure 2.6: Spin Torque Diagram. The ferromagnetic layer both acts as a spin filter, and is acted upon by the polarized incident electrons. The angular momentum lost by the incident electron is gained by the moment, reflected here as a torque that acts to bring the moment into alignment with the incident current.

deed occur, but for now we will operate with the assumption that the means employed to fix the magnetization in place are sufficiently robust that there is negligible change in its direction. However, some electrons incident on the fixed layer from the spacer layer will be scattered backwards towards the free layer, but with the spin orientation opposite that of the fixed layer, as shown in Figure 2.6. These spin-polarized electrons are then incident on the free layer, but now the spin torque promotes the antiparallel orientation. Current in one direction stabilizes the low resistance parallel state while current in the opposite direction stabilizes the high resistance antiparallel state. Thus, the spin-transfer system is a good candidate for a memory element, with small currents performing a read operation via GMR and large currents performing a write operation via spin-transfer. Figure 2.7 shows both kinds of switching for a device at low temperature.

The first indirect measurements of spin-transfer effects were done at Michi-

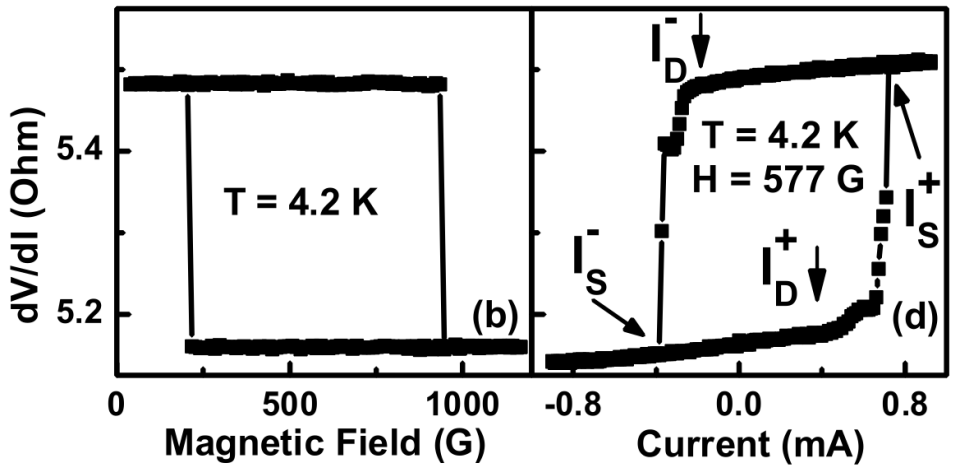

Figure 2.7: Field and current-based switching at low temperature. From Krivorotov.[8]

gan State University in 1998[9] in Co/Cu multilayers, which produced peaks in the differential resistance that were attributed to spin waves excited by spin-transfer. Soon after, the first spin-transfer systems capable of magnetic reversals were made at Cornell: Co/Cu/Co trilayers made small by nanoconstriction[10] and fully patterned nanopillars.[11] In 2003 the first observation of spin-transfer generated microwave dynamics[12] was made at Cornell.

2.3.1 Equations of Motion

In 1955 Gilbert[13] modified the Landau-Lifshitz Equation[14] for the motion of a magnetic moment $\mathbf{M}$ in an effective field $\mathbf{H}_{eff}$ by changing the form of the damping term to produce the now common Landau-Lifshitz-Gilbert (LLG) equation:

$$\dot{\mathbf{M}} = -\gamma_0 \mathbf{M} \times \mathbf{H}_{eff} + \frac{\alpha}{M_s} \dot{\mathbf{M}} \times \mathbf{H}_{eff} \tag{2.1}$$

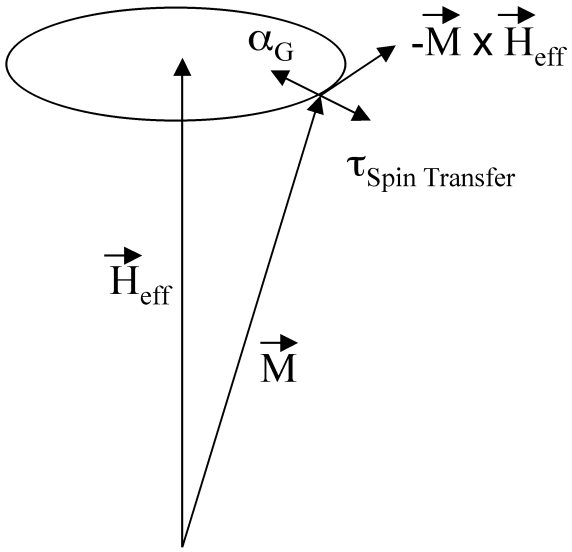

Figure 2.8: The spin-transfer torque can directly oppose the damping.

where γ_0 is the gyromagnetic ratio and α is the Gilbert phenomenological damping parameter. The first term describes procession around the effective field, while the second term has the system relaxing toward equilibrium. To account for the spin-transfer effect, Slonczewski[15] and Berger[16] added a third term to the LLG equation in 1996:

$$\dot{\mathbf{M}} = -\gamma_0 \mathbf{M} \times \mathbf{H}_{eff} + \frac{\alpha}{M_s} \dot{\mathbf{M}} \times \mathbf{H}_{eff} + \left(\frac{\gamma_0 \hbar}{e} \right) \frac{g(\theta) I}{V} \hat{\mathbf{M}} \times (\hat{\mathbf{M}}_2 \times \hat{\mathbf{M}}) \qquad (2.2)$$

where I, is the spin current polarized by M_2 (the fixed layer), V is the volume of the free layer, θ is the angle between the two layers, and g is a polarization function that depends on geometry and composition.

Note that, since spin torque involves the transverse component of the incident spin, there will be no torque acting on a layer oriented directly opposite to spin polarization of the incident current. However, the thermal fluctuations that are always present above absolute zero will eventually push the system out of this metastable state and allow the spin torque to take effect.

The spin-transfer term and the damping term point in opposite directions for the proper direction of the current, as shown in Figure 2.8. For this reason the spin-transfer torque is often described as a negative damping term, allowing the magnetization to spiral away from H_{eff}. If the damping should exactly cancel the spin-transfer torque at some angle, creating an effective 'zero damping' out of this dynamical equilibrium, then a stable precession at that angle will result. See Figure 2.9. If the spin torque is larger than the damping, switching will eventually occur.

Indeed, the critical current for the onset of spin-transfer-generated phenomena such as switching and dynamic precession can be estimated by calculating the current at which the spin-transfer torque first exceeds the damping term. As formulated by Sun,[17] the equation for the critical switching current is:

$$I_c = \frac{\alpha}{p}\left(\frac{2e}{\hbar}\right)(VH_kM_s)\left(1+\frac{2\pi M_s}{H_k}+\frac{H}{H_k}\right) \tag{2.3}$$

where α is the damping parameter, p is the spin polarization, V is the volume of the free layer, H_k is its uniaxial anisotropy field, M_s is its saturation magnetization , and H is the net field external field (set to zero in our experiments as we use an applied field to cancel the dipole field from the fixed layer). As we see in Eq. 2.3, the critical current varies directly with the Gilbert damping parameter α.

Figure 2.10 shows a phase diagram at low temperature. When the field is in the hysteretic region both parallel and antiparallel orientations are stable. If the applied field and current direction promote opposite states, then microwave dynamics can result from this dynamical equilibrium.

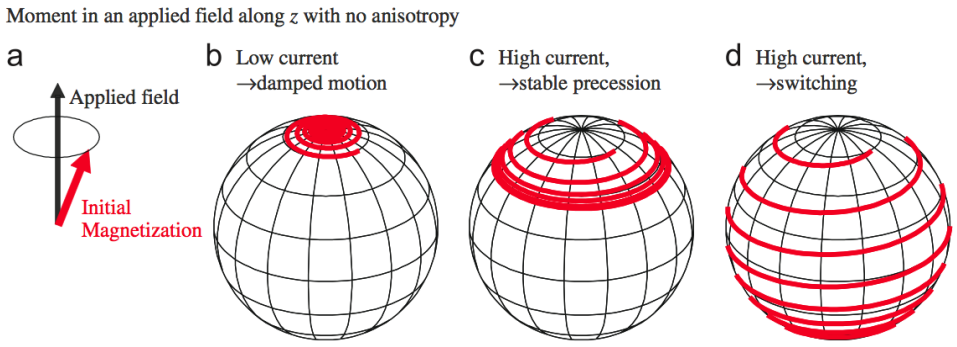

Figure 2.9: Trajectories of spin-torque-driven dynamics: a) The initial condition, possibly the results of thermal fluctuations. b) If damping is larger than the spin torque, the system returns to equilibrium. c) If the spin torque cancels the damping, stable precession can result. d) If the spin torque is larger than the damping, it can switch the state. From Ralph.[18]

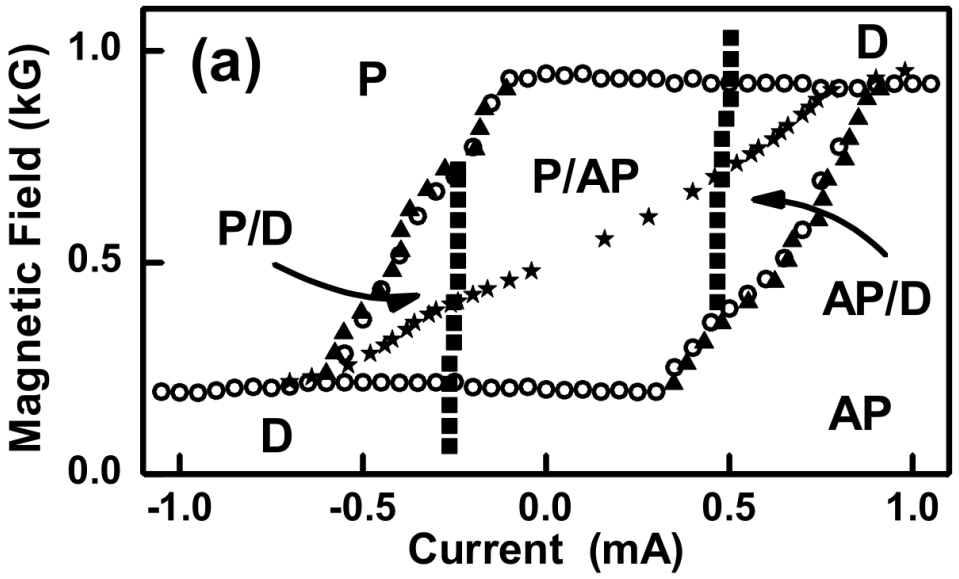

Figure 2.10: Phase Diagram for a Py nanopillar at 4.2 K. The stable states are Parallel (P), AntiParallel (AP) and Dynamics (D). Within the hysteretic region there can be switching between states, but at large enough field or current only one state is stable. From Krivorotov.[8]

2.4 About Alpha

Within the Gilbert phenomenological damping parameter hides a considerable amount of complicated physics. Alpha represents the sum of many competing processes, both intrinsic and extrinsic. There is considerable variation in both the value and dependence on various parameters, such as temperature or resistivity [19], even within the ferromagnetic transition metals.

Most theories involve temperature dependence through τ, the electron orbital lifetime, or its inverse, the scattering rate τ^{-1}. Processes that vary as τ such as the breathing Fermi surface model[20] are termed "conductivity-like", while processes such as spin-flip scattering that vary as τ^{-1} are "resistivity-like". As τ goes roughly as $1/T^2$,[21] conductivity-like behavior at low temperature and resistivity-like behavior at high temperature can combine for a fairly flat temperature dependence around room temperature.

Electron-phonon interactions mediated by spin-orbital coupling can produce spin-flip scattering.[22] Even ordinary scattering can relax the magnetization, as spin-orbital coupling causes the Fermi surface to depend on the magnetization direction, and this is reflected as scattered electrons (from collisions with lattice defects (e.g., phonons) [21]) repopulate it. [23] [24] [25] Magnons can also scatter off conduction electrons, which again relax to the lattice by spin-orbital coupling,[26] [27] [28] or decay to electron-hole pairs. [29] There are also extrinsic contributions such as two-magnon scattering [30] and spin-pumping[31], in which a movement in a ferromagnetic layer creates spin accumulation that can be dissipated in nearby layers (spin sinks). Two-magnon scattering does not play a large role in thin Py films. [19]

Good quantitative agreement from a general physical model remains elusive, even in recent work. [29] It is important to note that whatever the dominant process for damping ferromagnetic transition metals may be under a given set of conditions, the intrinsic damping processes all involve spin-orbital coupling as angular momentum is lost to the lattice, and can be enhanced via doping with terbium, and its large spin-orbital coupling.

2.5 Expected Temperature Dependence of the Terbium Contribution to Damping

Terbium has a high amount of spin-orbital coupling, which allows magnetic excitations such as magnons to be dissipated as phonons, greatly enhancing the magnetic damping. Our data and that of NIST[32] show a strong increase in the damping from Tb at temperatures below room temperature. This increase in α should directly increase the spin-transfer critical currents, but we will need a more precise model to explain the variation with temperature.

Kittel[33], along with De Gennes and Portis[34], discuss rare earth irons such as terbium substituted for yttrium in in an Yttrium Iron Garnet lattice (YIG, $Y_3Fe_5O_{12}$), a system in which the terbium ions couple individually to the majority lattice. They begin by considering the iron garnet lattice (A) and the Tb lattice (B) and by comparing the experimentally measured Weiss constants[35] λ to judge the relative strength of the exchange energies involved. Since $\lambda(Fe) = 15000 > \lambda(Fe - Tb) = 1100 > \lambda(Tb) = 36$ they treat the Fe lattice as fixed, the Tb ions as individually coupled to the larger lattice, and concentrate on the Fe-Tb interaction. We are guided in our analysis of the Py-Tb

system by their work: since their theory does not depend on the details of the exchange interaction or other material parameters of YIG (such as the presence of oxygen), we can apply it to our magnetic system. Below the Curie temperature, the relevant regime in these experiments, the Py atoms are strongly coupled to each other, and the Tb atoms still have comparatively weak interactions among themselves, and can be treated as independently coupling to the Py lattice. Their calculation for YIG shows τ/T as the temperature dependence of the FMR linewidth, and hence damping:

$$\Delta\omega \approx (N_B/N_A)\omega_{AB}^2\tau\hbar\omega/kT \tag{2.4}$$

De Gennes, Kittel and Portis give a qualitative explanation. [34] Consider the magnetic system losing energy to a thermal bath at temperature T (with $\bar{p}$ as its thermal average quantum number of the phonons of frequency ω) by exciting one additional phonon. The rate of this transition is proportional to $\bar{p}+1$, while the rate of the reverse process to pump energy back into the magnetic system by losing a phonon is proportional to $\bar{p}$. The net flow out of the system is proportional to the fraction of the transitions

$$\frac{(\bar{p}+1)-\bar{p}}{(\bar{p}+1)+\bar{p}} \approx \frac{1}{2\bar{p}} \approx \frac{\hbar\omega}{2kT} \tag{2.5}$$

where we have used [36]

$$<\bar{p}>= \frac{1}{exp(\frac{\hbar\omega}{kT})-1} \approx \frac{\hbar\omega}{kT} \tag{2.6}$$

in the limit that $kT >> \hbar\omega$.

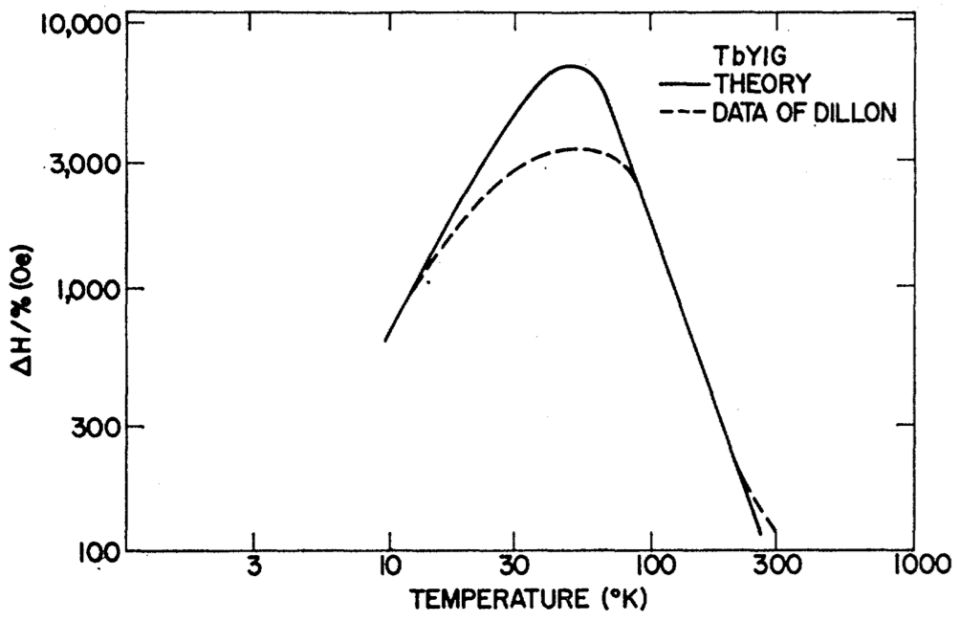

Figure 2.11: Linewidth of terbium-substituted yttrium iron garnet as a function of temperature. From Seiden[37]

Dillon [38] measures ΔH in the garnets directly, and finds qualitative agreement with the temperature dependence, but not the frequency dependence. Seiden [37] incorporates both the slow-relaxation and the fast-relaxation theories, and achieves good agreement on either side on the peak, as shown in Figure 2.11. Note that when we consider ΔH at temperatures higher than the peak, we recover the 1/T temperature dependence derived by Kittel [34].

Dionne and Fitch [39] extend Seiden's work for rare earth doping of garnets with elements other than terbium, and find good agreement. They consider the Fe and Tb damping as two independent processes using the Orbach paramagnetic model, and carefully treat the exchange couplings. Their calculation

$$\Delta H = \gamma^{-1}\left(\frac{\hbar\omega}{kT}\right)\left[AT^n + \zeta_0\left(\frac{(1-k_c)E^c_{ex}(T)}{E^c_{ex}(0)}\right)Be^{-D/KT}\right] \tag{2.7}$$

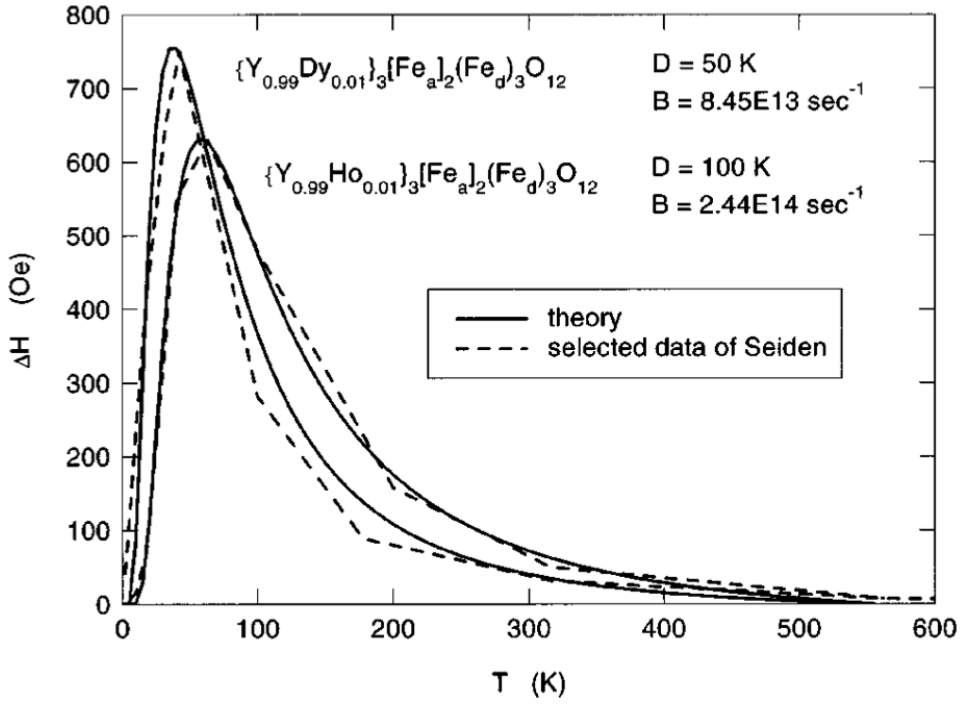

Figure 2.12: Comparison of theory [39] with selected data [37] of FMR linewidth as a function of temperature for $(Y_{0.99}Dy_{0.01})Fe_5O_{12}$ and $(Y_{0.99}Ho_{0.01})Fe_5O_{12}$. From Dionne and Fitch[39]

captures the peak well, as shown in Figure 2.12. Note that A is small enough to ignore in our system. At low temperatures (left of the peak) the rate is limited by the $(e^{-D/KT})$ relaxation time of the rare earth ions, while at higher temperatures (right of the peak) the rate limited by the $1/T$ factor accounting for the possibility of thermal energy flowing back into the magnetic system. Since this range is where our data lies, we will use the simplified form of the high-temperature limit and fit the data to $1/T$.

2.6 Why Nanoscale?

Let us briefly discuss why the effects and technologies discussed so far are so entwined with nanoscale fabrication. First and foremost, consider the z-direction, or thickness. Clearly, this dimension must be smaller than the spin-diffusion length for any of the spin-dependent effects to be significant. As this is ≈ 250 nm in Cu and shorter in the magnetic metals, reaching the nanoscale is necessary to observe these effects.

There is another effect to consider. Any physicist, asked to describe how a current in a wire would affect a magnetic moment, would not begin with spin-transfer, but with the Oersted field the current produced, circulating the wire. At the boundary of the wire of radius R carrying current I, this field is

$$B = \frac{\mu_0 I}{2\pi R}\hat{\theta} \tag{2.8}$$

while the spin-transfer effect scales as $1/R^2$, so spin-transfer only dominates at small dimensions. Furthermore, smaller devices have more uniform magnetizations, and spin-transfer better couples to uniform modes than the explicitly non-uniform Oersted field.

Finally, the heat effects also call for small devices, as the current density required to switch, ranging from 10^5 to 10^9 mA/cm^2 depending on device design, would produce enough Joule heating to destroy a device not small enough to be uniformly well coupled to a much larger thermal mass.[40]

All of this explains why spin-transfer and GMR required modern thin-film deposition and nanoscale fabrication techniques in order to be discovered and studied.

CHAPTER 3

FABRICATION AND MEASUREMENT METHODS

3.1 Fabrication

We begin with 3 inch silicon wafers that have been oxidized on their surface so as to be insulating. The metallic stack is then sputtered onto the wafer. The sputtering chamber is pumped down to a base pressure of 3×10^{-8} Torr , so that the magnetic layers will not oxidize during deposition. During deposition, 1-2 mTorr of Ar gas is allowed into the chamber through vents in the sputtering guns, where high DC voltage converts it to a plasma that knocks free atoms off the target material. Computer-controlled shutters above the guns precisely limit the amount of time the wafer is exposed to the streams of excited atoms from the gun. Since the typical deposition rate is adjusted to be a few A/sec, the thickness deposited is accurate to within a fraction of a nanometer. The wafer is rotated during deposition to improve uniformity across the wafer, which is important as the six sputter guns are angled away from perpendicular.

The deposition rates for most materials were calibrated by performing profilometry on a 100-200 nm sample deposited through a photolithographically-defined grating. The Py-Tb alloys were calibrated by co-sputtering the Py and Tb guns at several different powers, then performing X-ray Photo-emission Spectroscopy (XPS) on the samples to determine their composition and linearly fitting the resulting concentration-power curve.

The metallic stack for a basic control sample is shown in Figure 3.1. The bottom Py only provides adhesion between the SiO_2 substrate and the metallic

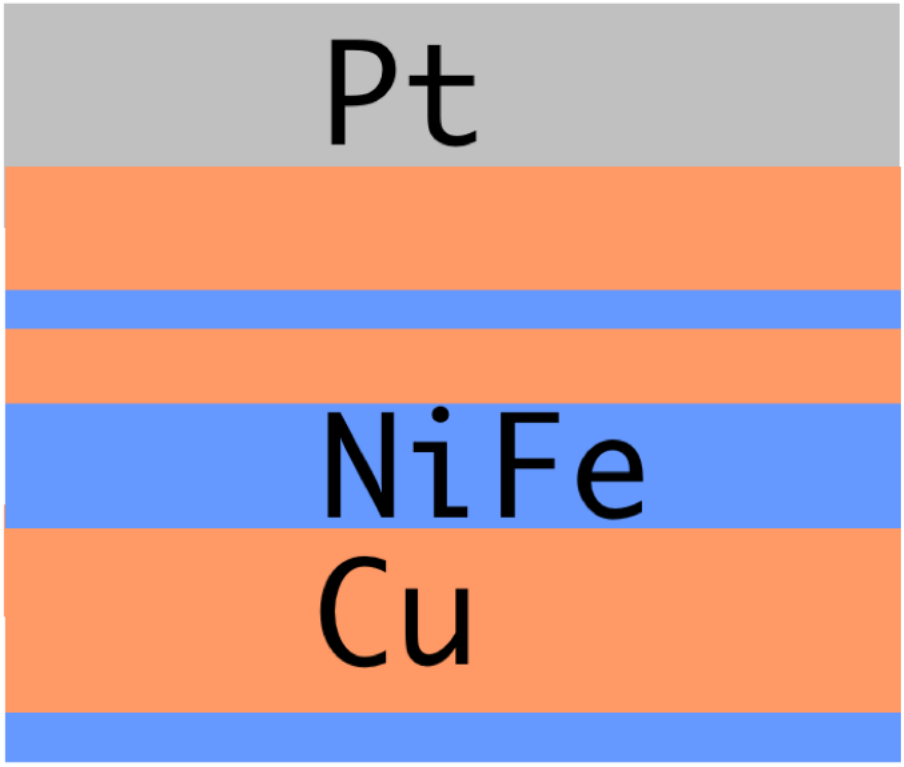

Figure 3.1: Sputtered layers for a control sample.

stack. The large Cu layer is for the bottom leads and is thicker, providing a margin of error for the etch that defines the pillars, which stops in this layer. The two Py layers and the Cu spacer between them form the core of the spin-transfer system under study. The top Cu layer serves to isolate the magnetic layers from the Pt, which can disrupt the magnetic structure and serves as spin sink. Finally, the capping layer (Pt, Au or Ta) protects the rest of the stack from atmospheric oxidization. The composition for the devices in this dissertation (in nm) is Py(4) / Cu(120) / Py (20) / Cu (10) / Free (5) /Cu (20) / Pt (30). The 5 nm free layer was either pure Py, as in the control sample, uniform Py-2% Tb alloy (referred to as low power Tb) or a sandwich of Py/Py-4% Tb alloy/Py (referred to as high power Tb) that has the same overall dose of 2% Tb, as shown in Figure

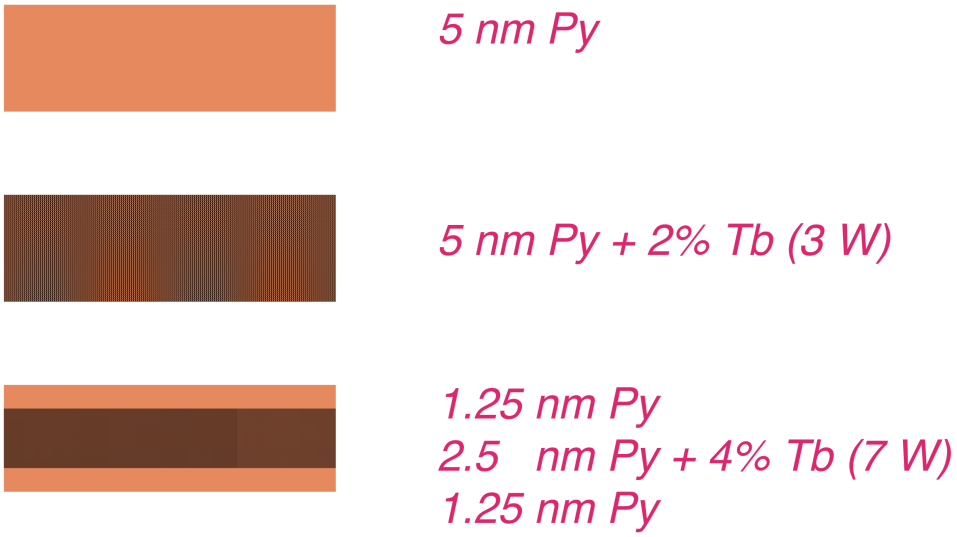

Figure 3.2: Three different free layers: the pure Py control, uniform Py-2% Tb alloy (referred to as low power Tb) or a sandwich of Py/Py-4% Tb alloy/Py (referred to as high power Tb). The Tb concentrations were measured by XPS.

3.2.

A roughly 50 nm film of carbon graphite is electron-beam evaporated above the capping layer. The carbon will serve as a mill mask during pillar definition later in the process. Immediately before being inserted into the vacuum chamber for evaporation, the wafer is heated on a hot plate to drive off any moisture the surface may have absorbed from the atmosphere. This moisture can interfere with the adhesion between the graphite and the capping layer.

The elliptical cross section of the pillar, shown in Figure 3.3, is defined by electron-beam lithography (e-beam). This particular size was used for the high power Tb samples, while 40 by 120 nm was used for the low power samples. Two different e-beam resists are spun on (950 K PMMA on top of 495 K PMMA) in order to create an overhang with the top layer, see Figure 3.4, promoting better lift-off. It is important to refrain from cleaning the wafer with acetone

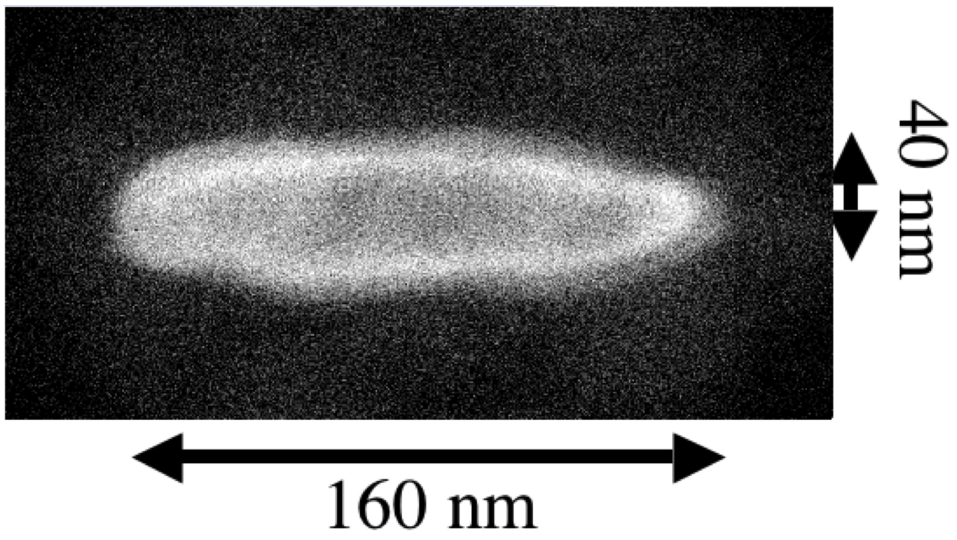

Figure 3.3: Cross section of typical device. Taken with an electron microscope.

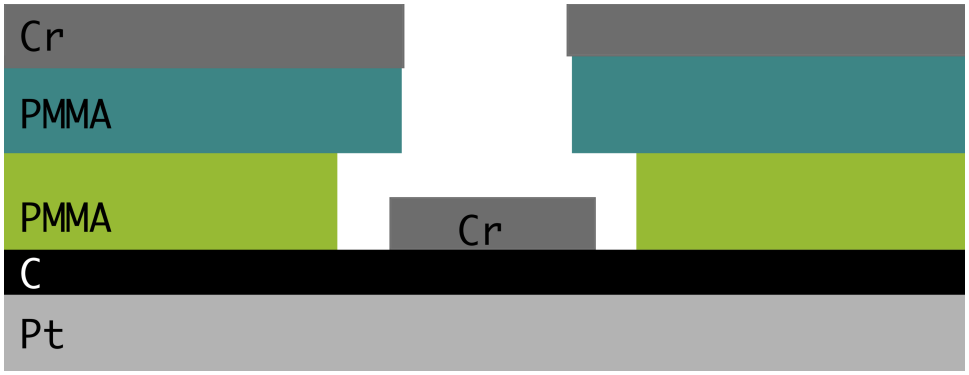

Figure 3.4: Bilayer E-beam Resist after Chrome Deposition. The chrome will protect a portion of the carbon during RIE etching.

while the carbon is exposed, as it can be damaged by exposure to the solvent.

The e-beam exposure with the VB6 tool is the most difficult and expensive portion of the fabrication process. Fortunately, the VB6 has several features to promote reproducibility, such as computer-controlled motion, and laser height correction. The exposure defines an array of ellipses, such as shown in Figure 3.3, along with several aliment marks so that the later photolithography step

can deposit leads around the ellipses. The exposure consists of two levels of organization. There is a 9 x 9 grid of identical squares. As shown in Figure 3.5, each square contains a 4 x 4 grid of devices (one ellipse each), along with some features to aid processing that will be described later.

After development for 1 minute in a dilute solution of Isopropyl Alcohol (IPA), there are holes in the resist where it has been exposed to the electron beam (ellipses and alignment marks). Through these holes we thermally evaporate 15 nm of chrome, as shown in Figure 3.4. After the e-beam resists and excess chrome are stripped away in an acetone bath, the wafer is placed into an O_2 plasma in a Reactive Ion Etcher (R.I.E). The islands of chrome protect the carbon beneath them, while the rest of the carbon is converted to gas by the plasma. This transfers the pattern from the chrome, which lifts off well from the resists, to the carbon, which does not. The color of the plasma is a bright blue while it is reacting rapidly with the carbon, but changes to a yellow-green when exposed only to the more inert metals and oxides remaining in the chamber. We record the length of this process as the carbon etch time (typically less than 2 minutes) to calibrate the length of the later etch, when we remove the remaining carbon thickness that was protected during this step.

Once the e-beam lithography and processing has finished defining the smallest features, photolithography can be used for the remainder of the fabrication. Photolithography is preferred over e-beam lithography for larger features as it is both faster and less expensive. Each of the six photolithography steps (each with its own associated mask) consists of the same sequence: spin on the photoresist and bake it; align the wafer with the 5x stepper photolithography tool using the alignment marks from the e-beam step; expose the pattern (which varies with

each step) to each of the 81 squares on the wafer; remove the exposed portion of the resist with developer; expose the wafer to a 15 sec O_2 plasma in the R.I.E. to remove any residue of resist exposed but not fully developed; process the patterned wafer (which varies with each step); then strip the resist, and any excess material from processing, with an acetone bath. The photoresist used is Shipley 1813, with the P10 adhesion promoter used in all steps except for the first two. The developer is 300 MIF for most steps, and a solution of 312 MIF and distilled water for the last two steps since these patterns are smaller and require a stronger developer. Whenever the wafer is exposed to acetone, such as during the resist stripping, it is washed in IPA before drying. While acetone dissolves resist and many other contaminants that might be in the wafer, it leaves a residue if dried directly.

The first photolithography pattern is used to define the bottom leads and top lead contact pads, as shown in Figure 3.6. The entire device is protected, while the area between devices is exposed so it can be milled away. The material is removed via an ion mill, in which Ar+ ions are accelerated in a vacuum chamber by a large voltage between two metallic grids, neutralized with electrons so as to be unaffected by any stray electron fields or image charges, and allowed to impact the wafer, violently ejecting the atoms on the surface. The wafer is cooled to 10 C and the Ar beam is periodically interrupted by a shutter to prevent the protective resist from overheating and baking, as the resulting cross-linking interferes with subsequent resist removal. The sample is again rotated during milling to improve uniformity, and tilted at an angle measured to minimize redeposition of the milled material onto the wafer. All of the metal sputtered onto the wafer in the non-protected regions is removed in this milling, electrically isolating the individual devices from each other, as well as isolating

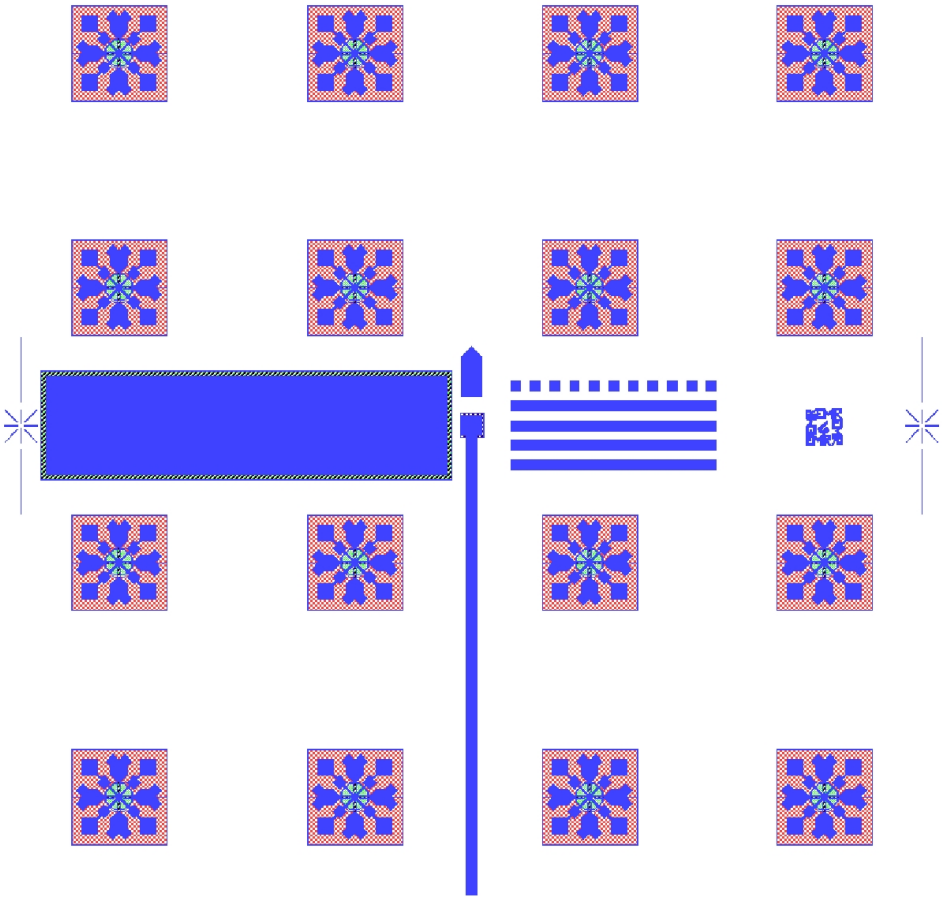

Figure 3.5: Schematic Diagram of Device Array. This pattern is repeated 81 times on a 3 inch wafer.

the bottom leads and pillar from the top lead contact pads. The mill is timed by observing though a portal in the vacuum chamber when the SiO_2 is visible (with a small additional margin for insurance) to ensure that all the metal has been removed.

The second photolithography step also involves ion milling. However, in this pattern (Figure 3.6) only the area around the pillar is exposed. The contact pad's capping layer is maintained so that no oxides form that might add to the contact resistance. This mill etches down the previously protected bottom leads and device area to remove the magnetic layers. However, the carbon

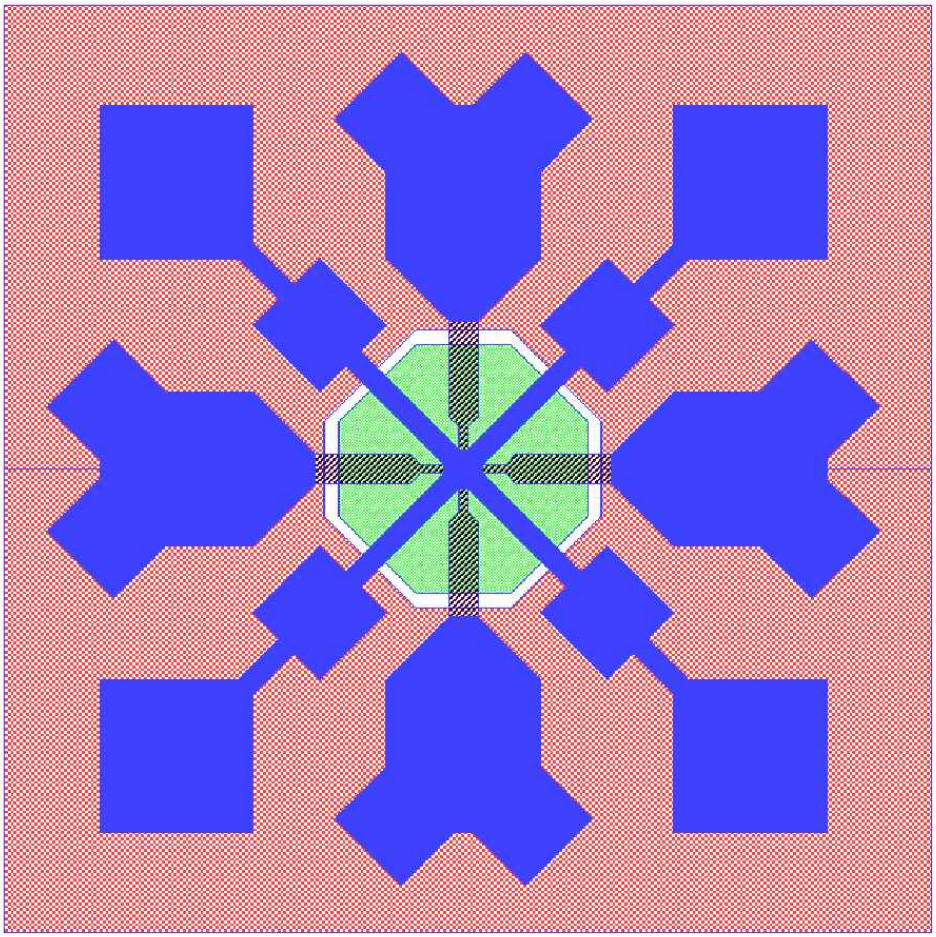

Figure 3.6: Diagram of a Single Device. The area protected by photoresist in Mask 1 is shown in solid blue. The octagon exposed to ion-milling by Mask 2 is shown in green. The top leads deposited with Mask 6 are shown in grey for reference. The pad pattern is chosen so that the probes can touch down from 8 different directions, and accommodates high frequency probes, which require three square pads in a shallow triangle,

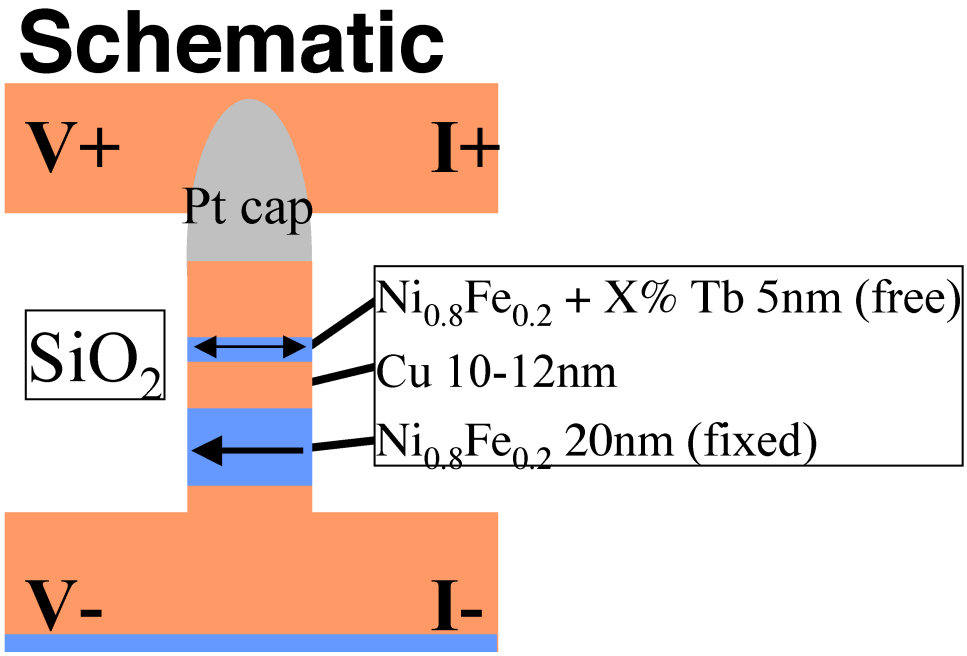

Figure 3.7: Cross section of a finished device. The walls of the pillar are defined by ion-milling, then encased in insulating oxide.

mask protects the area under the ellipse, producing a nanopillar with an elliptical cross-section that is smaller than can be defined with photolithography alone. (Figure 3.7) The mill is timed to stop in the bottom Cu layer using etching rates for the various materials previously calibrated with the grating and profilometry method described earlier. The bottom Cu layer is made thick to make this timing easier. After stripping the resist, the height between the top of the capping layer and the lowest etched area of the bottom leads is measured using profilometry to assess the height of the pillars at both the edge and center of the wafer.

In addition to measuring directly the height difference between various portions of a device, we also verify the profilometry measurements on arrays defined for this purpose. The arrays are useful for quickly generating a large number of measurements and better statistics, and many ridge pairs can be mea-

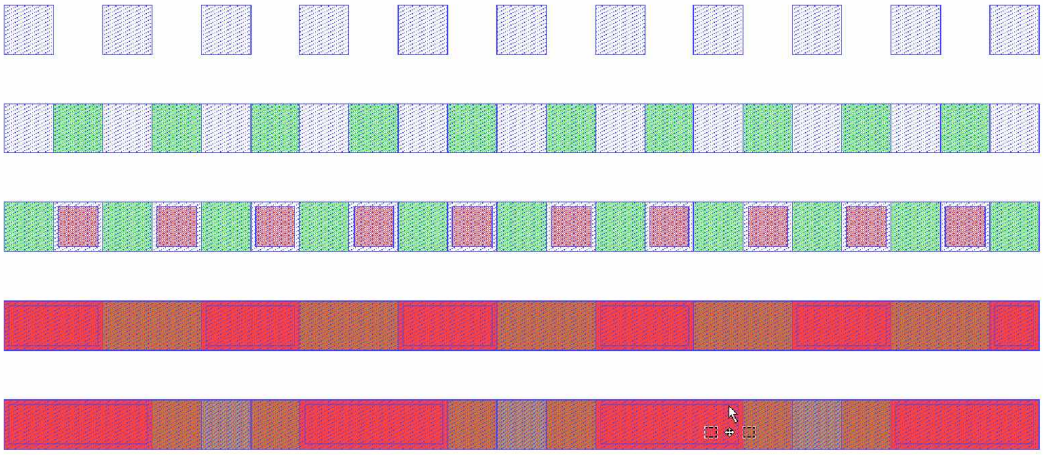

Figure 3.8: Profilometry Array. Each color corresponds to a different mask, and each row is used for one of the five profilometry measurements.

sured in a single pass of the profilometer's probe, and there is less difficulty positioning on the array than in the narrow window afforded by the actual devices. If the measurements from the array and a few actual devices agree, then they can be used. There are five rows: one for each profilometry measurement. As Figure 3.8 shows, each row is protected and exposed by the same sequence of masks that the relevant feature in the device receives.

At this point Scanning Electron Microscopy (SEM) is used to measure the area of the various pillars. This can be difficult as the intense energies used for the imaging can distort or destroy the pillars. One solution to this problem is to create a redundant set of pillars, as we do with our array near the center of each die, shown as a small blue square in Figure 3.5. The square with the array is connected electrically to the edge of the die, and thus the rest of the wafer, so that it can be electrically grounded. This was done in an attempt to limit the damage during SEM exposure due to charge build-up. However, there did not seem to be substantial improvement. A further problem with the array approach arises

from the proximity effect. Because the electrons used in patterning the devices do not travel straight down to be absorbed perfectly by the e-beam resist, the dose a portion of resist receives is partially dependent on the dose given to a portion in close proximity. For this reason, bringing the 16 devices closer together, as we do in the test array, will cause secondary effects on their shape, reducing the accuracy and usefulness of measuring the array to gain information about the sizes of the actual devices. To correct for these possible errors, actual devices are sacrificed and measured both near the center and edge of the wafer. By moving between measurement locations very quickly, and by determining focus and abjuration-corrections before imaging the actual device, it is possible to achieve accurate, complete images before the device is deformed. These images are analyzed to determine the cross-sectional area and aspect ratio of the pillars, and compared to the array measurements to check the extent of the proximity effect in a given pattern.

Now that the bottom leads and the pillar have been defined, all that remains is to electrically insulate the side of the pillar and attach the top of the pillar to the top leads contact pads. The delay between the pillar definition and the oxide deposition should not be too long, as sidewall oxides will impair device performance. [41]Electrically contacting to the top of the pillar reliably, without shorting to the magnetic layers, requires precision milling and consistent oxide thickness. For these reasons, the process is more involved than it would be otherwise, with several deposition and smoothing steps to create a more uniform oxide layer.

The bulk of the insulating oxide is deposited by Plasma Enhanced Chemical Vapor Deposition (PECVD). However, the pillar must first be protected from

the caustic environment of the PECVD chamber, so a 5 nm layer of SiO_2 is thermally evaporated on the wafer first. While evaporation is safer than PECVD, it is much slower, and is unsuited to the half micron thicknesses required, necessitating this two-step process. During the PECVD process, the wafer is kept at 170 °C for around 10 minutes. While many PECVD recipes call for much higher temperatures, we limit the process temperature to 170 °C as we are concerned about interlayer mixing at elevated temperatures. The cut-off temperature was chosen at 170 °C to mirror the temperature used to bake the e-beam resist, another crucial step. The PECVD exposes the heated wafer to a mixture of nitrous oxide and silane gas excited to a plasma in order to quickly deposit a conformal oxide. The thickness deposited is very sensitive to the deposition conditions and can vary considerably between runs, so we target a thickness of three times the pillar height to insure full coverage.

Once the PECVD oxide is deposited, the sides of the pillar are insulated electrically. However, the height of the oxide on top of the pillar is higher than that of the surrounding area, making it difficult to expose the top of the pillar without also exposing the sides, leading to the magnetic layer being shorted across. This problem is solved by planarizing the oxide with a shallow angle (15°) ion mill. While such a milling can increase roughness by exaggerating any trenches on the surface, it serves our purpose, as we know the predominant feature of the landscape is a lone peak, which will be milled from the side as the wafer rotates. The success of the planarization is verified by Atomic Force Microscopy (AFM), which excels at measuring thickness differences. While the actual pillar is too small to be well-imaged in the AFM as it is comparable to the sharpness of the AFM tip, the presence or absence of the oxide bump is easier to detect. Again, measurements are made at both the center and edge of the wafer, to account for

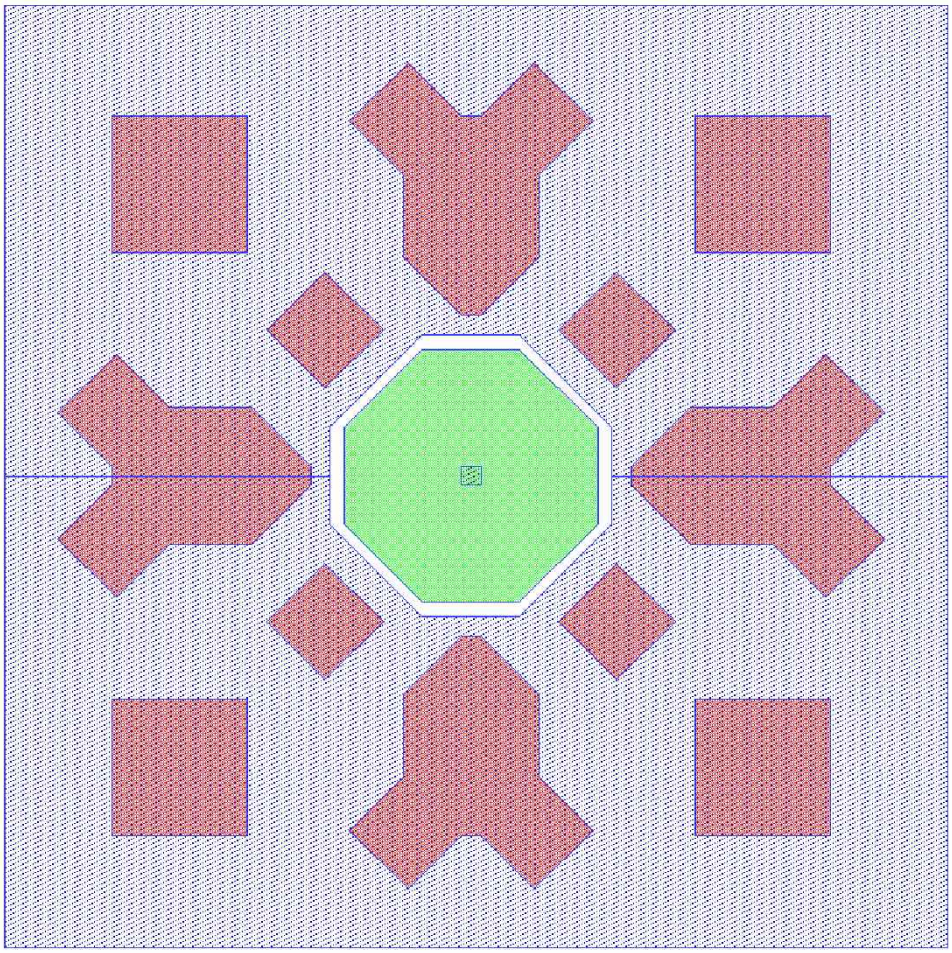

Figure 3.9: Mask Layout. The area exposed to ion milling by Mask 2 is shown in green. The areas exposed to HF chemical etching by Mask 3 are shown in pink. The area protected by photoresist with Mask 5 is shown by blue shadow.

non-uniformity.

The third photolithography step removes the oxide from the contact pads. With pads exposed (see Figure 3.9) and the rest of the oxide protected by the resist, the wafer is dipped in a buffer oxide etch of Hydrofluoric acid, which efficiently etches SiO_2 while leaving the capping layer unaffected. After the resist is stripped, the height difference between the oxide and the top of the capping layer over the bonding pads is measured, giving an estimate of the

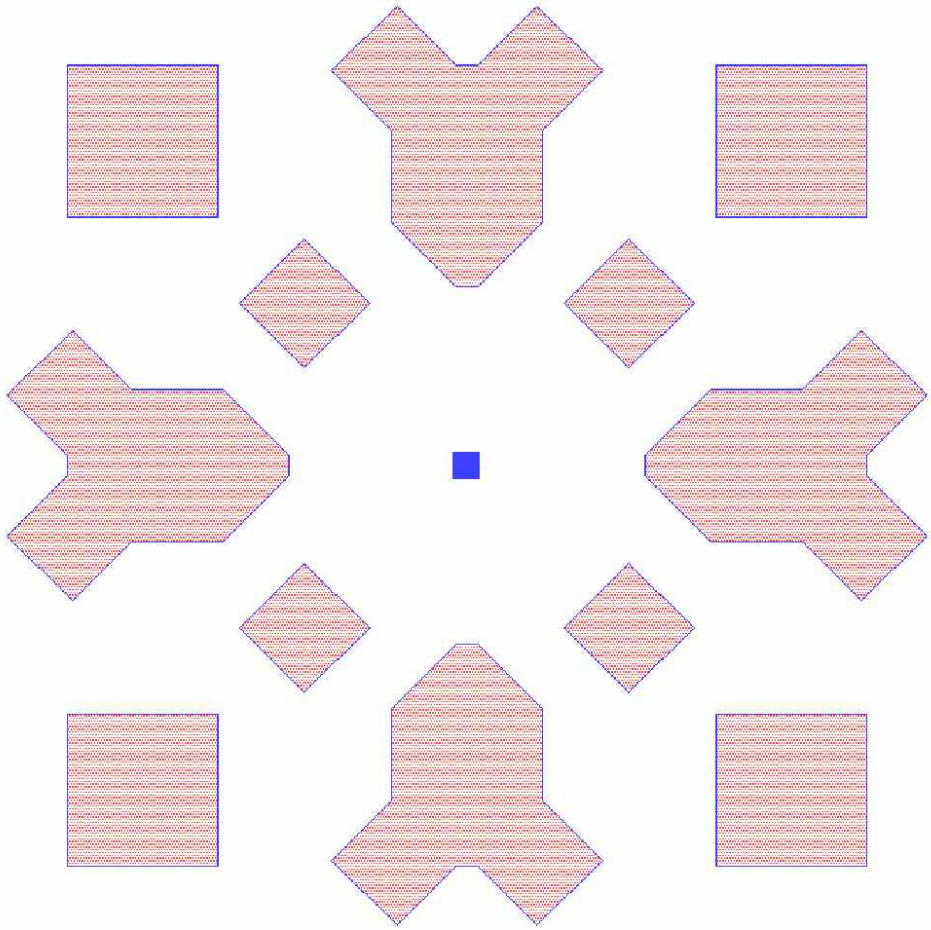

Figure 3.10: Mask Layout. The area exposed to ion-milling by Mask 5 is shown in solid blue. The bonding pads from Mask 3 are shown in pink shadow for location reference.

height of the oxide on top of the pillar remaining after planarization.

The fourth photolithography exposes the areas where the top and bottom leads overlap to a 100 nm oxide evaporation, to guard against any fabrication errors in the previous steps that might allow for a shorting of the two leads together. The area over the pillar is protected against deposition to avoid adding oxide that will just be removed later. After the resist is stripped, the oxide height above the pillar is again indirectly measured, but this time the entire wafer is mapped out, to account for spatial non-uniformity in processing.

If the oxide measured above the pillar is thicker than 80 nm, as is often the case, then an optional fifth photolithography step must be done. Otherwise, there is a risk that the bonding pads will be completely milled away in milling after the final photolithography step. This optional step opens a small hole above the pillar (see Figure 3.10) that allows only that part to be ion-milled, causing the oxide above the pillar to be selectively removed and brought closer to the height of the bonding pads, avoiding the above mentioned problem. After the resist has been patterned, developed, and descummed, the wafer is ion-milled as described above, with a 40 mA beam current and at 20° from normal, then stripped of resist and remapped with the profilometer to establish the new, reduced oxide height over the nanopillar.

Once the height of the oxide above the pillar has been mapped across the wafer and verified to be less than 50 nm, then the final photolithography mask, for top lead deposition and contact, is patterned as shown in Figure 3.11. The usual sequence of spin resist, expose pattern, develop resist, and RIE to remove scum is followed. At this point the wafer is cleaved into small chips, so that the spatial variation in the oxide thickness may be addressed. Typical chip sizes vary from 2x1 die sections to 3x4 die sections, depending on the extent of the variation in oxide thickness. The cleaving should not be done before this step as it considerably complicates the photolithography.

The chip is then ion milled to remove the remaining oxide above the pillar, and to expose the remaining carbon mask or possibly the bare capping layer. The length of this mill is timed using the wafer map, and an etch rate that is tuned for each wafer. Starting with a rate of 1.8 $\mathring{A}$/sec, the rate is adjusted up and down until the chips can be contacted reliably. If too high a rate is used,

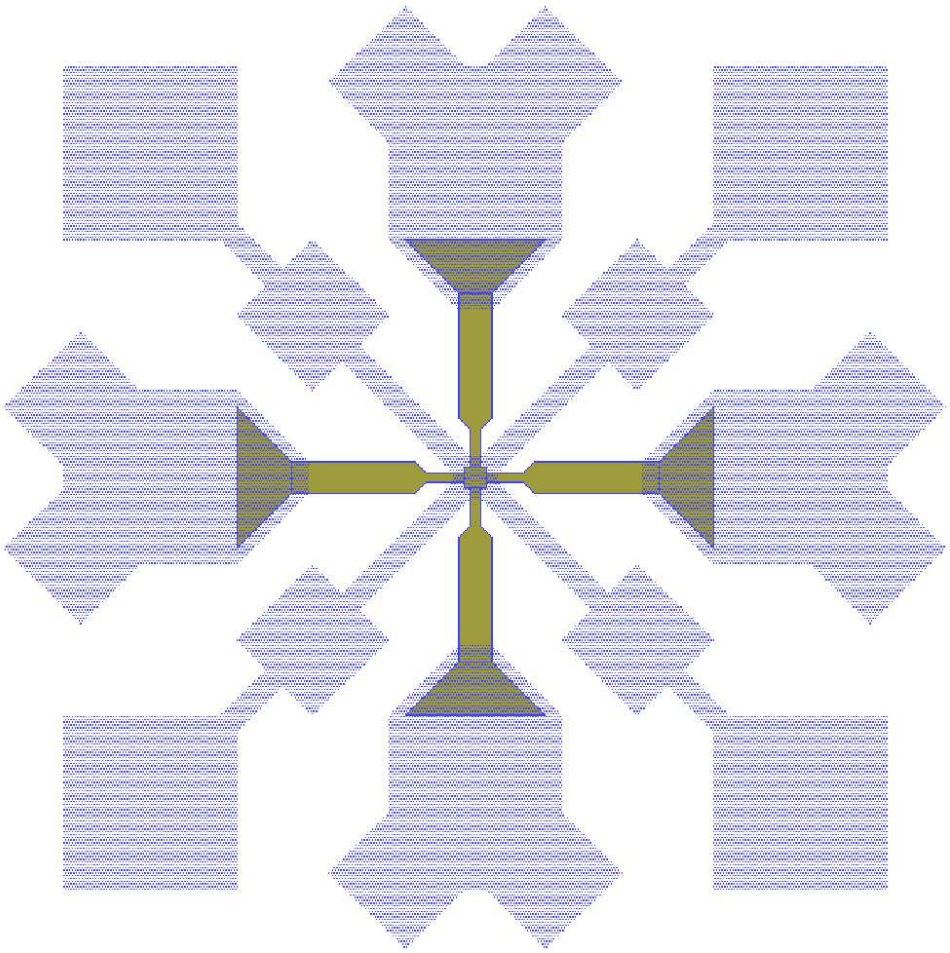

Figure 3.11: Mask Layout. The area exposed to ion-milling and copper deposition by Mask 6 is shown in solid gold. The bonding pads from Mask 1 are shown in blue shadow for comparison.

then the mill will be too short and oxide will remain between the pillar and the top lead, leading to a electrical measurement of open circuit. If too low a rate is used, then the mill will be too long, causing not only the oxide on top of the pillar to be removed, but also a portion of the oxide on the side of pillar. If the oxide height drops below the top magnetic layer, then the devices will be magnetically shorted by the top lead, and show no resistance variation in response to magnetic changes. Note that if the devices on the die vary considerably in size and shape, then there may not be one rate that provides good contact to all

pillars. In this case, the process is simply iterated for each pillar type. Fortunately, a 9x9 grid provides plenty of chances. Typically, a workable rate will be found by the fourth try.

Once the oxide has been removed, the chip is placed in the RIE to remove any carbon remaining on the top of the pillar. The etch time is three times as long as was necessary to remove the unmasked carbon earlier, typically around a total of four minutes. The chip is now ready for top lead deposition. Immediately before the copper is deposited, a short, low-power ion mill is used to remove any surface oxide on the metal. The copper is then sputtered or ion beam deposited less than a minute later, without breaking the 10^{-6} Torr vacuum in the chamber. After the resist and excess copper is removed in the usual fashion, the chip is ready to be measured.

3.2 Electrical Measurements

There are two ways to address the fabricated devices electrically. Wirebonding cold welds wires between the contact pad for the device leads and a matching pad on a chip carrier, which can then be plugged into the apparatus. Probes are made of a semi-flexible material that bends slightly as it runs along the pad. Wire-bonding takes an extra step and can only measure a few devices at a time. Probe contact is quicker, less violent, and can be easily reversed. The last quality is important for switching between measurements optimized for low-frequency and ones optimized for high frequency. The disadvantage is the probe contact is less robust, and can create a varying contact resistance when large fields cause the probe arms to bend, or thermal expansion and contraction during temper-

ature measurements moves the probes. Probe contact is also more dependent on the cleanliness of the pad surface than the wire-bonding method. Because of the higher device throughput and yield, the probe method is now used predominantly, but devices that show promise under probe measurements are sometimes wire-bonded for further study.

DC switching measurements are done using a Wheatstone bridge, shown in Figure 3.12. If R_{Large} is much larger than the sample resistance, then the current flowing through any resistor will be $I = V_{In}/R_{Large}$ and the measured voltage becomes $V_{Out} = I(R_{Sample} - R_{Match})$ where R_{Match} is chosen to match the sample resistance. This technique allows us to subtract out the relatively large offset resistance R, and focus only on the change in resistance ΔR in response to field and current. As a practical matter, this means we can employ much higher gain without overloading any of the amplifiers. A small AC signal on the order of 1 kHz and 10 to 50 μA is used to probe the differential resistance with a lock-in amplifier, while a DC current on the order of mA, applied at the same time, causes the actual spin-transfer switching. A 1 $k\Omega$ resistor is put in series with the current source to prevent the small AC sense current from being shorted by the current source, as the device resistance is much smaller than 1 $k\Omega$.

The resistance alone provides much information on the quality of the sample. We expect the devices discussed in this thesis to be on the order of a few ohms, so a sample over 100Ω would be the result of a fabrication error such that some part of the device is "open", with no low resistance path between each of the leads and the magnetic device, while a device under 1Ω is likely a "short", either because some stray bit of metal is actually shorting the top and bottom leads together, bypassing the magnetic device, or because ion-milling for too

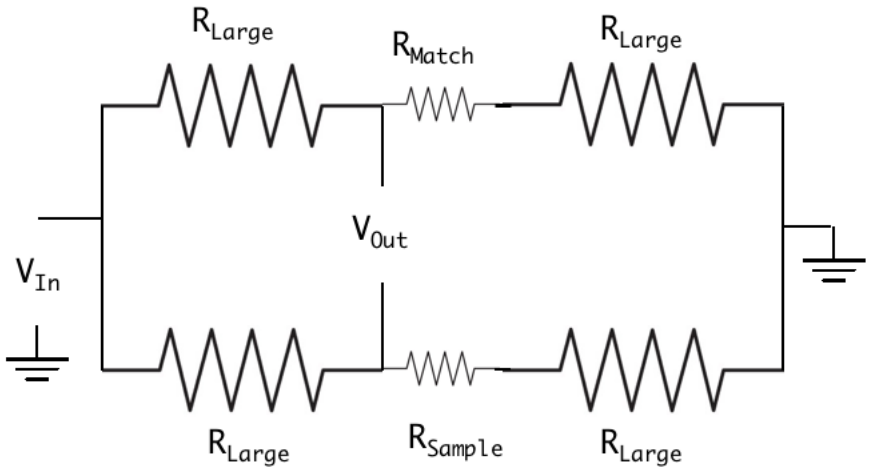

Figure 3.12: Circuit diagram of the Wheatstone bridge used to measure the small resistance change.

long in the photolithography step 5 has entirely removed one or more of the magnetic layers. Shorts are confirmed with a field scan.

Before applying any spin-transfer level currents to a new device, a field scan is performed to asses the device's quality. In the measurements discussed here, the magnetic field is always applied along the major axis of the ellipse that defines the device shape. The positive direction is chosen arbitrarily. By sweeping the applied magnetic field through large positive and negative values, we can determine if the device is magnetically responsive, and measure the change in resistance ΔR. Then sweeping a minor loop, as in Figure 3.13, we can measure the coercive field $H_c = 0.5\ \Delta H$, and the dipolar field H_d, equal to the offset of the loop from zero field. We expect the ΔR for full reversal in the current driven spin-transfer switching to match the ΔR from the field sweep. During current

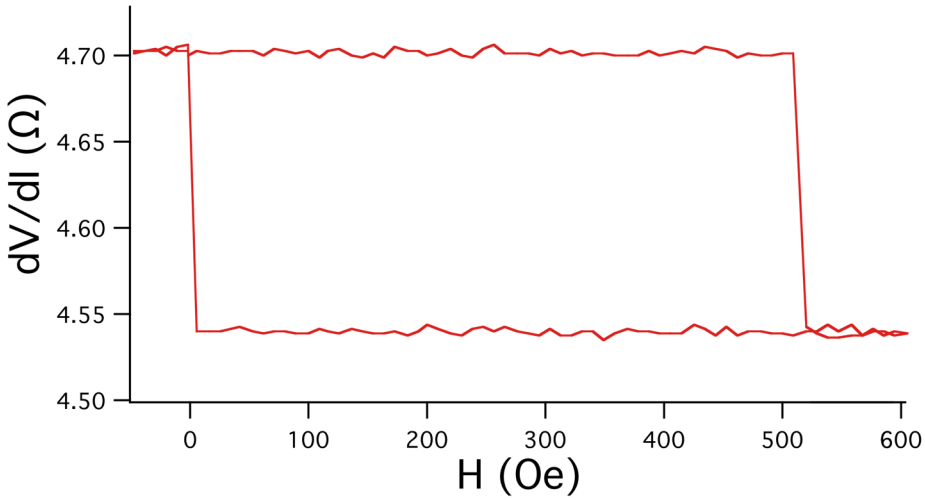

Figure 3.13: Resistance vs. Magnetic Field for a typical device's minor loop. Here $R = 4.54\Omega, \Delta R = 0.16\Omega, H_d = 265$ Oe, and $\Delta H = 505$ Oe.

scans, the field is usually set to be the center of the minor loop, as this value will cancel out the dipole field from the fixed layer, and approximate zero external field.

The switching process for a DC current sweep at a non-zero temperature is thermally activated, rather than purely "state determined". In the macrospin approximation, we may say that the magnetic moment of the free layer received occasional random 'kicks' from the thermal bath. As the DC current is increased, the energy barrier between the initial and the switched state becomes smaller, until one of the thermal 'kicks' is sufficient to move the system over the barrier, into the stable switched state. See Figure 3.14. The random nature of the 'kicks' lead to a variation in the time (and therefore current) of switching. Since a slower ramp rate of the DC current will cause the system to spend more time between any two given DC current values, thus subject to a larger number of thermal 'kicks', the measured value of the switching current will also be re-

duced. Thus both the mean and standard deviation of the switching currents depends on the DC current ramp rate, and both are temperature dependent, even before thermal magnetic effects are considered.

The above-described measurement set-up involves numerous wires, which can act as antenna for stray signals and create pick-up noise. After several tests, it was clear that this noise was adding to the effective temperature of the device, causing premature switching in a manner similar to the previously-discussed thermal excitation. To combat this effect, simple low-pass filters are placed on both cables leading to the probes. Obviously, these filters are not used for high-frequency measurements. Tests with and without the filters show that the measured critical currents are measurably lower without the filters. To avoid damaging the samples with static discharge, the inputs to the device are shorted together when not in use. Rotary make-before-break switches are used, so that there will be no spark during the transition.

3.3 Low Temperature Measurements

Measurements of magnetic damping in response to field excitations in terbium-doped bulk permalloy films show a much larger Gilbert damping parameter at lower temperatures. [32] Accordingly, we have investigated the temperature dependence of the spin-transfer driven switching in our terbium-doped permalloy nanopillars in order to examine more clearly the effect of the rare earth doping.

Low temperature measurements were performed both on wire-bonded devices mounted in dewars and on devices contacted in a cryo-probe station. In either case liquid nitrogen was used to cool samples to temperatures above its

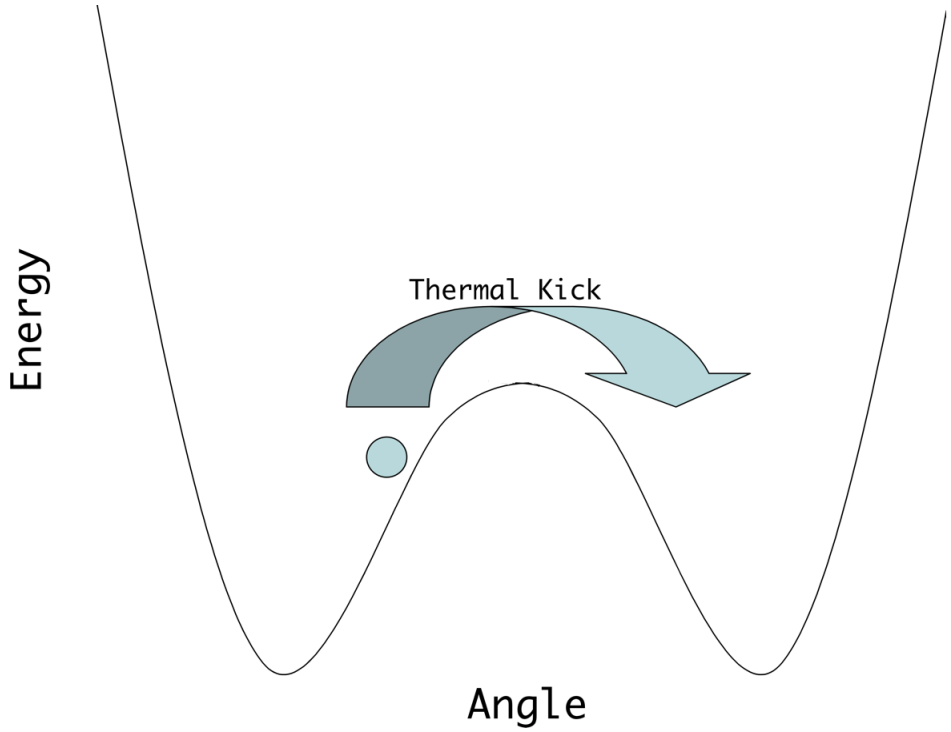

Figure 3.14: Thermal energy is able to excite the system into transition at a lower current than is possible with spin-torque alone. This figure is also shown as Figure 4.6.

77 K boiling point, and liquid helium was to cool samples as low as 4 K. To achieve intermediate temperatures, a nearby heater was used on a PIV feedback loop with a thermocouple to counterbalance the coolant. Samples were given at least 15 minutes after the measured temperature stabilized to reach thermal equilibrium before measurement.

CHAPTER 4

SWITCHING RESULTS

Terbium-doped permalloy nanopillars require substantially higher DC currents to induce switching behavior than in undoped control samples, as shown in Figure 4.1. Both switching currents (parallel to antiparallel and the reverse) are higher in the 2% Tb sample by approximately a factor of three. Both the control sample and the terbium-doped sample have a thickness of 5 nm and a cross sectional area of 0.005 μm^2, so they can be placed on the same scale. This increase is attributed to Terbium's large spin-orbital coupling allowing magnetic excitations to be dissipated as heat more effectively, keeping the system in equilibrium longer.

4.1 Temperature Dependence Discussion

Previous work done at NIST [32] shows that the additional damping provided by Tb doping is even stronger at lower temperature. Figure 4.2 shows the results for extended thin Py films with the damping measured in response to short field pulses at various temperatures. Note that while the control sample has slightly lower damping at lower temperature, the terbium sample shows a sharp increase. We also replot this data on a linear graph in Figure 4.3, so that it can be easily compared to a 1/T dependence.

To discuss the effect of cooling on the Tb-damping interaction, we must first isolate it from other temperature effects that affect switching current. Let us return to the formula for critical current (Eqn. 2.3) and include temperature-dependent terms.

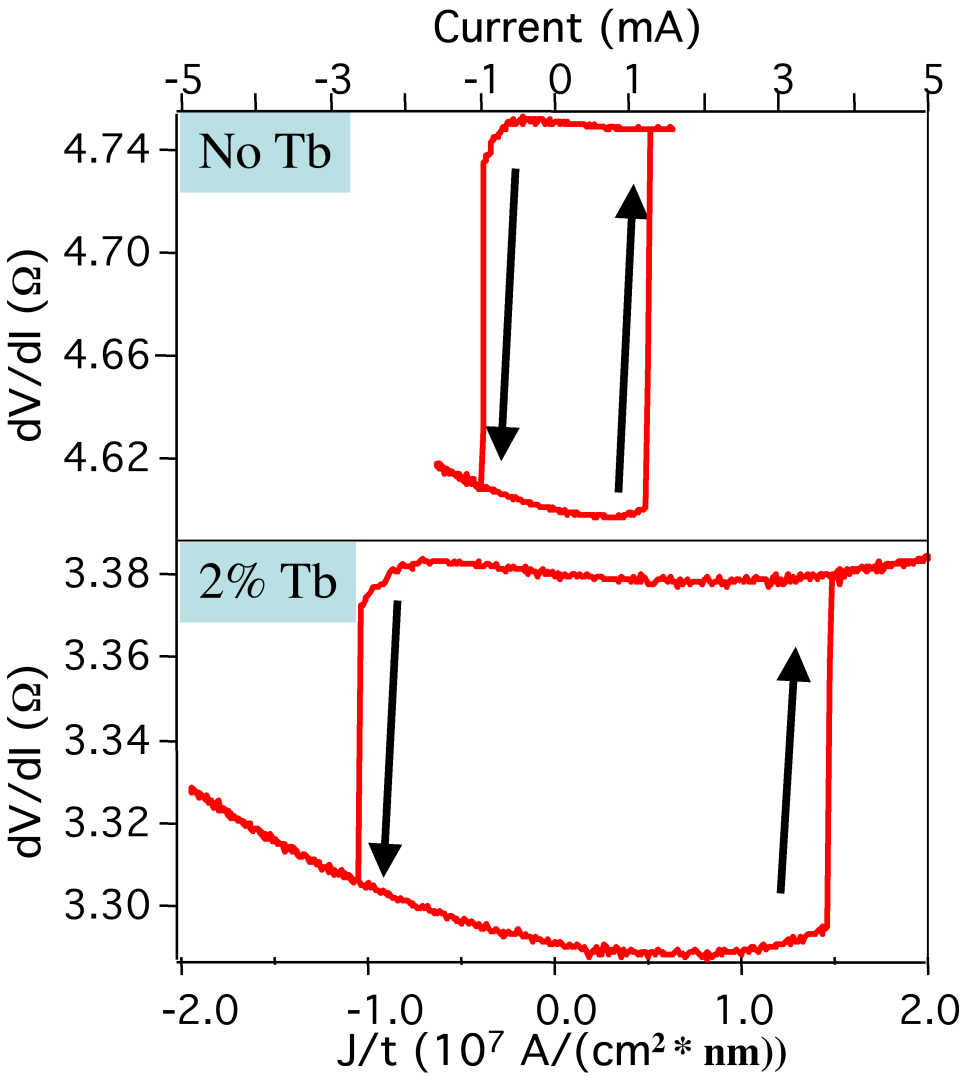

Figure 4.1: Hysteretic switching in Tb-doped and control samples.

$$I_c(T) = \frac{\alpha(T)}{p(T)} \left(\frac{2e}{\hbar}\right) V\, M_s(T)\, (H_k(T) + 2\pi M_s(T)) \tag{4.1}$$

Since $H_k(T)$ varies as $M_s(T)$, we can reduce the above to focus on the damping:

$$I_c(T) \propto \alpha(T) \frac{M_s(T) M_s(T)}{p(T)} \tag{4.2}$$

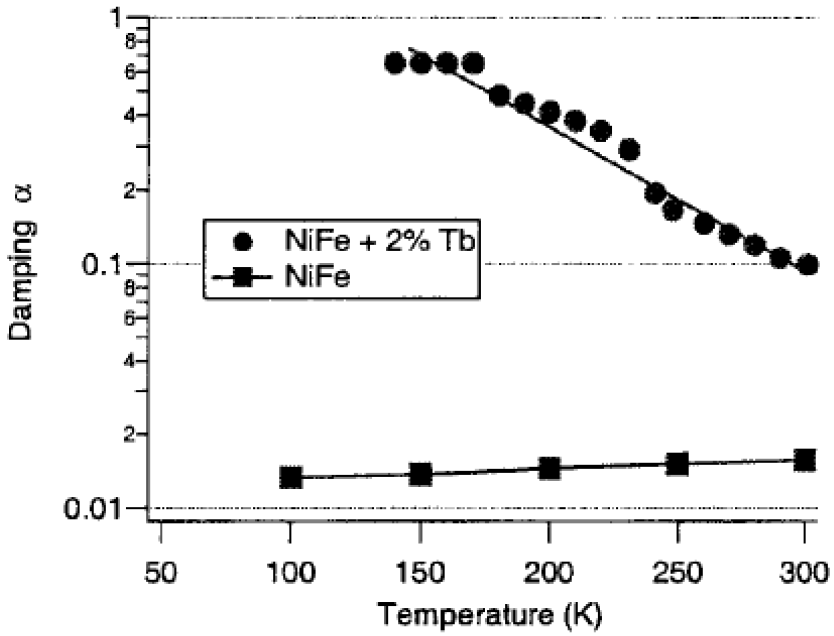

Figure 4.2: Previous work done at NIST [32] shows that the additional damping provided by Tb doping is stronger at lower temperature, while pure Py shows only slight temperature dependence.

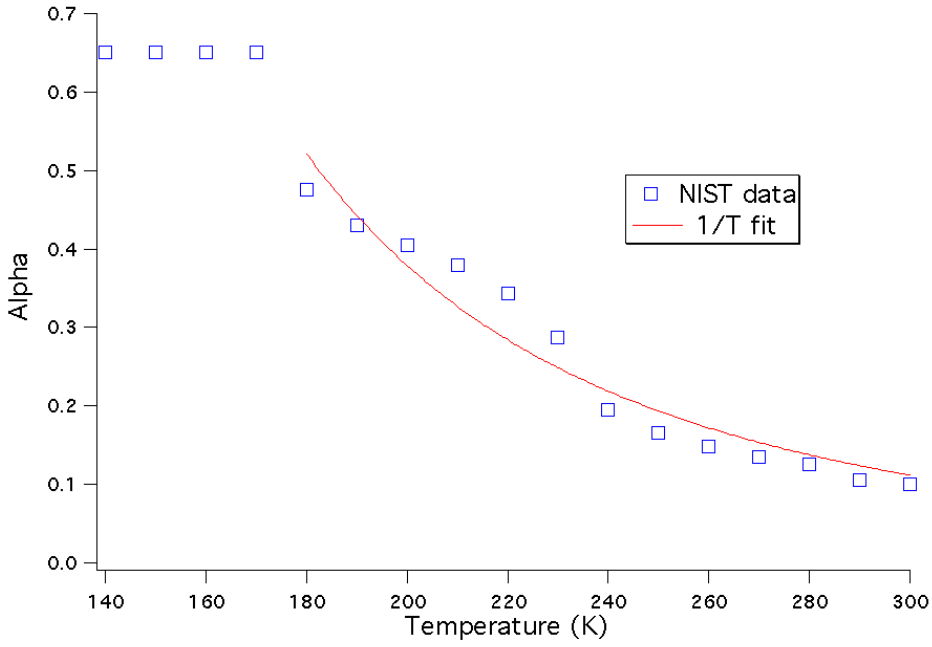

Figure 4.3: When replotted on a linear axis, the data from NIST [32] shows good agreement with a 1/T temperature dependence.

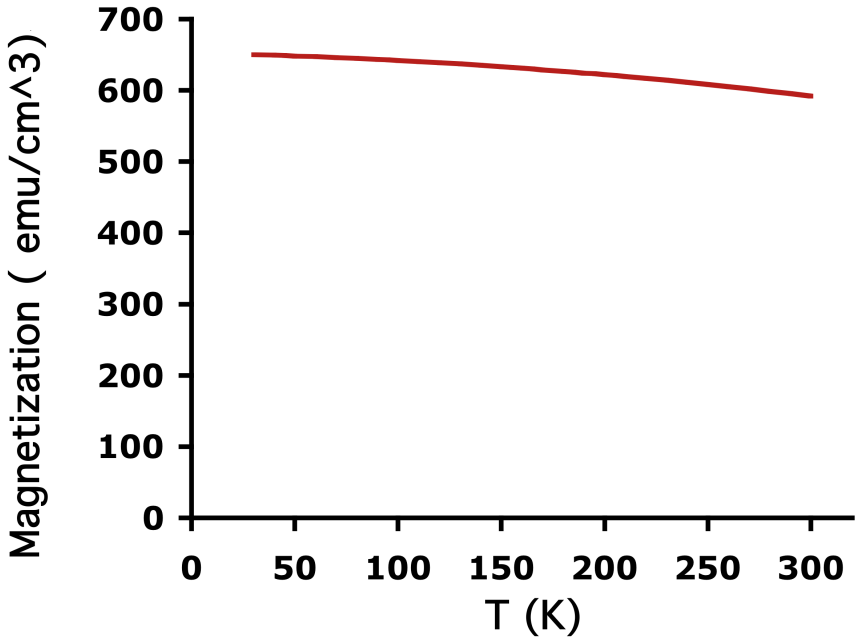

Figure 4.4: The change of the magnetization with temperature of an extended Py film was measured in a SQUID and found to match theory well.

Figure 4.5 shows the increase of ΔR at low temperatures, roughly a factor of two higher than room temperature. This we attribute to the increase in p at lower temperature, along with decrease in the lead resistance. Increases in M_s and p at lower temperature will affect I_c in opposite ways, offsetting each other for a reduced net effect. The change in magnetization with temperature can be measured directly with a SQUID, as shown in Figure 4.4, and is therefore easily accounted for. Thus, we should expect the temperature dependence of the critical current to match that of the Gilbert damping parameter α.

There is another factor of temperature dependence we have not yet addressed, and it goes to the heart of the difference between critical current predicted by theory above, and the switching current measured by experiment.

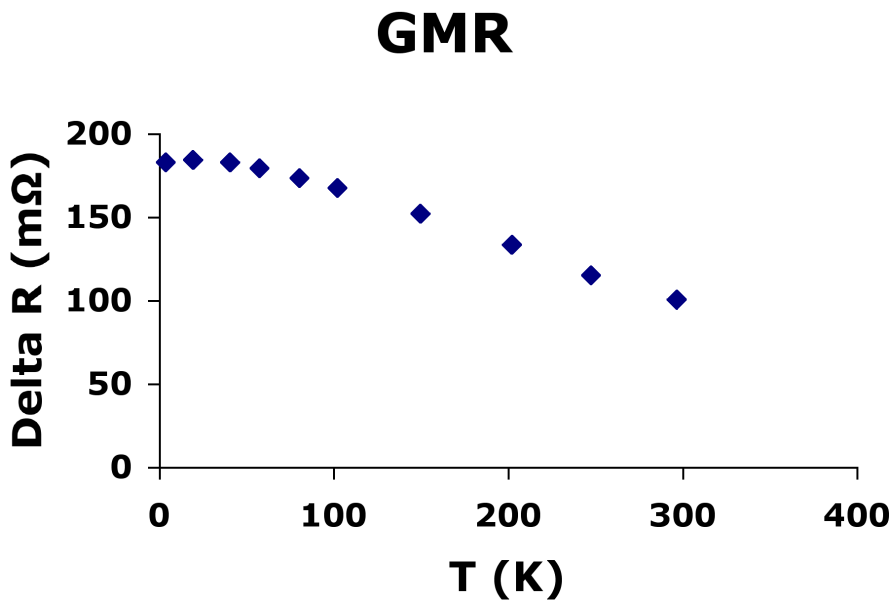

Figure 4.5: The GMR of the Py nanopillars increases at lower temperature with the larger spin polarization, as expected.

This is the effect of thermal promotion. The theory discussed above finds the current where the torque exceeds the damping and the system is driven from equilibrium. However, at real temperatures, thermal energy can contribute to the effect. Consider the parallel and anti-parallel states as minima in a double potential well, as shown in Figure 4.6. With no current, the thermal energy may be unlikely to excite the system over the barrier within a certain amount of time. As the current is increased, the spin-torque causes the potential to shift linearly[8] lowering the effective barrier. Unless the temperature is zero, as in the theoretical case, or the time window too short for a thermal kick to be likely, as with the shortest pulses, the system will be kicked over the barrier by a thermal excitation before the barrier goes to zero. Clearly, the strength of this thermal effect depends on temperature. This process introduces event-to-event variation, as well as a dependence on current ramp rate or pulse length and a

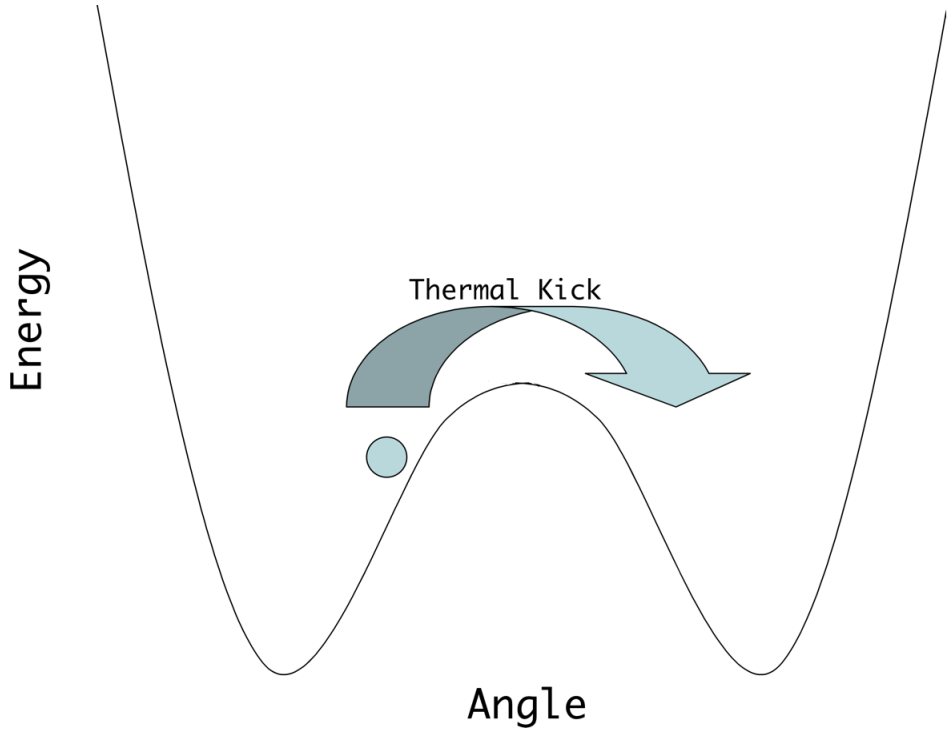

Figure 4.6: Thermal energy can excite the system over the barrier at a lower current than that at which the barrier is flat.

temperature dependence independent of the magnetic effects discussed above. Fortunately, we can model it and factor it out in our analysis.

Braganca et al.[42], extending earlier work,[8] [43] address these issues using a Kurkijarvi [44] treatment of Neel-Brown thermally-activated magnetic reversal due to a spin torque. If we consider the temperature dependence of their formula, we find

$$\langle I_c(T) \rangle = I_{c0} \left[1 - \frac{k_B T}{E_b(T)} \ln \left(\frac{k_B T I_{c0}}{\tau_0 E_b(T) \dot{I}} \right) \right] \tag{4.3}$$

Assuming a fluctuation attempt time τ_0 of 1 nsec, we vary the ramp rate $\dot{I}$ of the applied current at room temperature, average over 20 scans at each rate, and

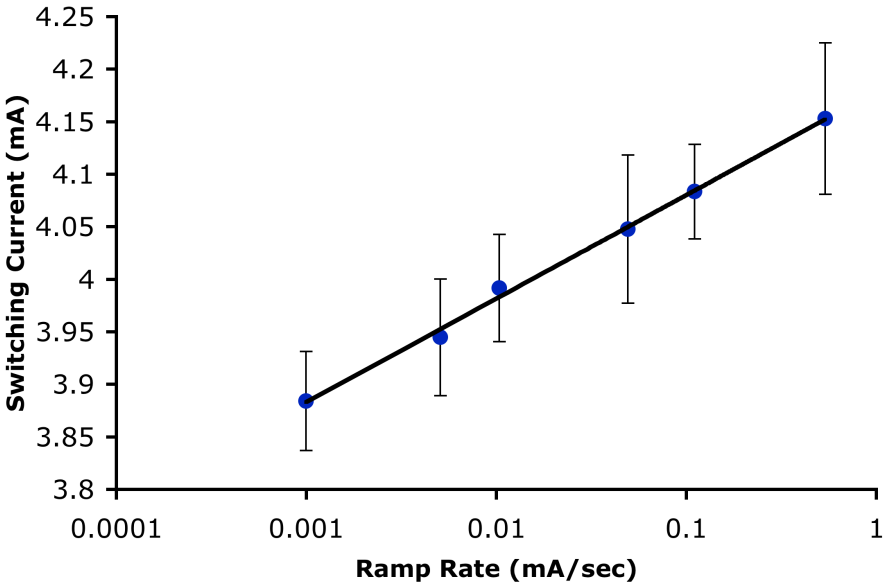

Figure 4.7: Ramp rate data for switching a high power Tb device to the anti-parallel state. The points shown are the average switching current from 20 attempts, and the error bars are the standard deviation. The fit shown gives a barrier of 2.9 eV.

fit to this formula to calculate I_{c0}, the critical current in the absence of thermal promotion effects, and E_b, the energy of the barrier, as shown in Figure 4.7. Once we have these values at room temperature, we can use this same formula to extrapolate what the critical current would be at lower temperatures under this thermal promotion model. The barrier itself will vary with temperature, and can be scaled by the square of the magnetization[8]. We will return to these concepts later when we discuss the pulsed measurements.

As shown in Figure 4.8, this simple thermal promotion model captures the temperature dependent behavior of the Py control samples quite well. This agreement gives us confidence that we have accounted for the leading order in the temperature dependence, so we can make an accurate comparison to the

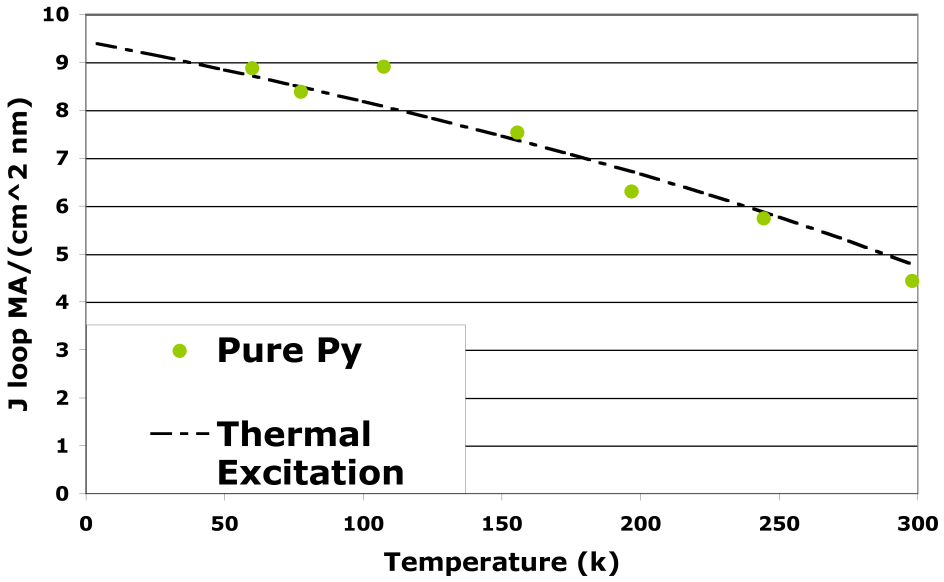

Figure 4.8: Switching current data from the pure Py control samples agrees with the thermal promotion model, indicating that the damping effects not related to Tb are well accounted for.

effects caused by the terbium. If we examine the terbium-doped samples in the same way, as shown in Figure 4.9, we see that the enhancement of critical current for switching at lower temperatures is much larger than can be accounted for with thermal promotion. Figure 4.10 shows the temperature dependence for both types of terbium-doped samples in comparison with the control samples. We can subtract the predicted increase from thermal promotion in order to isolate the contribution of the terbium to the damping. However, there is an additional effect to address first.

The terbium doping can make the critical currents so high that the Joule heating from the switching current significantly affects the temperature. This gives the switching curves a parabolic shape, as shown in Figure 4.12. This effect is especially pronounced at lower temperatures, where the critical currents are

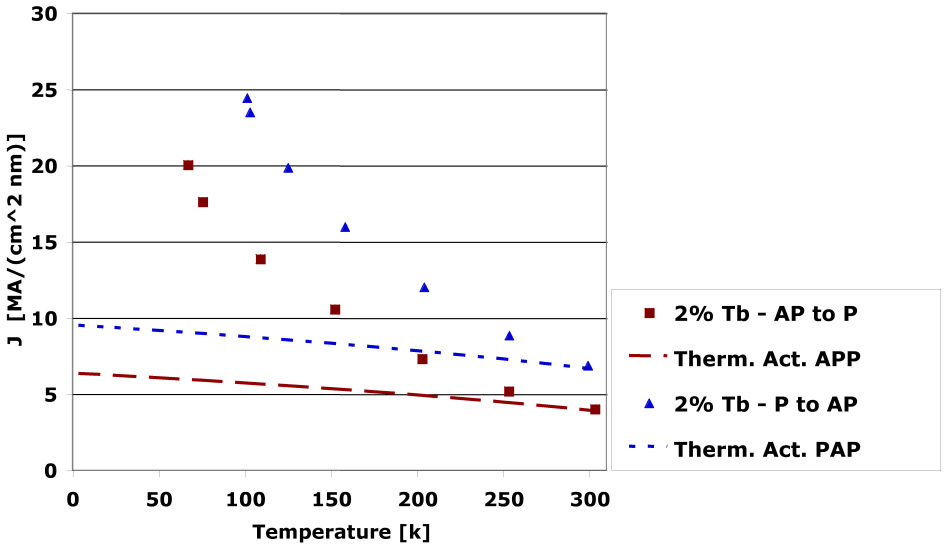

Figure 4.9: The Tb samples show switching current behavior in both directions that departs dramatically from the model, demonstrating the strong temperature effects of the rare-earth-assisted damping.

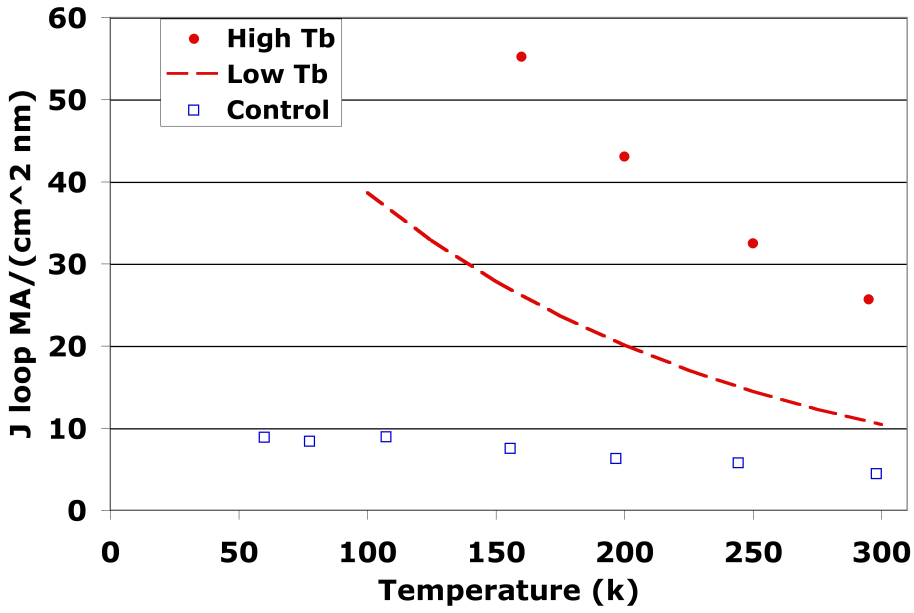

Figure 4.10: Both concentrations of Tb show larger critical currents at low temperature.

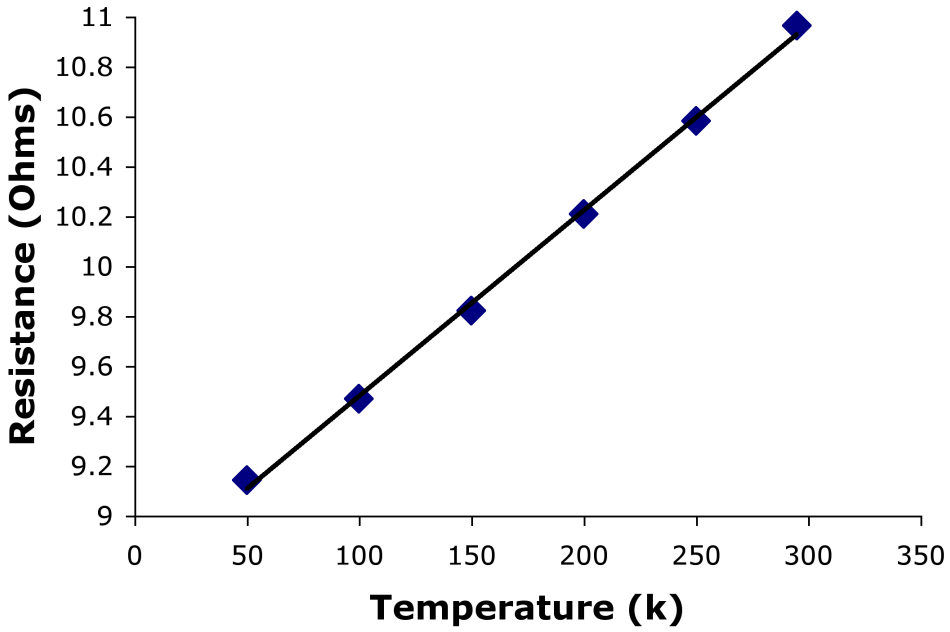

Figure 4.11: Calibration curve for resistance vs. temperature taken at zero DC current.

higher and bath temperatures lower. Thus, to accurately study the temperature dependence of the spin-transfer damping, we must account for this discrepancy between the bath temperature and the device temperature. We do so by using the device itself as a thermometer.

First, we plot the offset resistance of the Wheatstone bridge (see Figure 3.12) as a function of temperature and fit this to a line, as shown in Figure 4.11. This gives us a calibration in the absence of Joule heating. Then we need only note the resistance at the switching current to find the relevant temperature. Some care must be taken, however, as $\frac{dV}{dI}$ can start to show the influence of dynamics near the switching current. When this occurs, we simply fit the differential resistance curve using data from before the dynamics are observed, then extrapolate to the switching current. To find the coefficients, we fit the data to:

$$\frac{dV}{dI} = AI^2 + BI + C \tag{4.4}$$

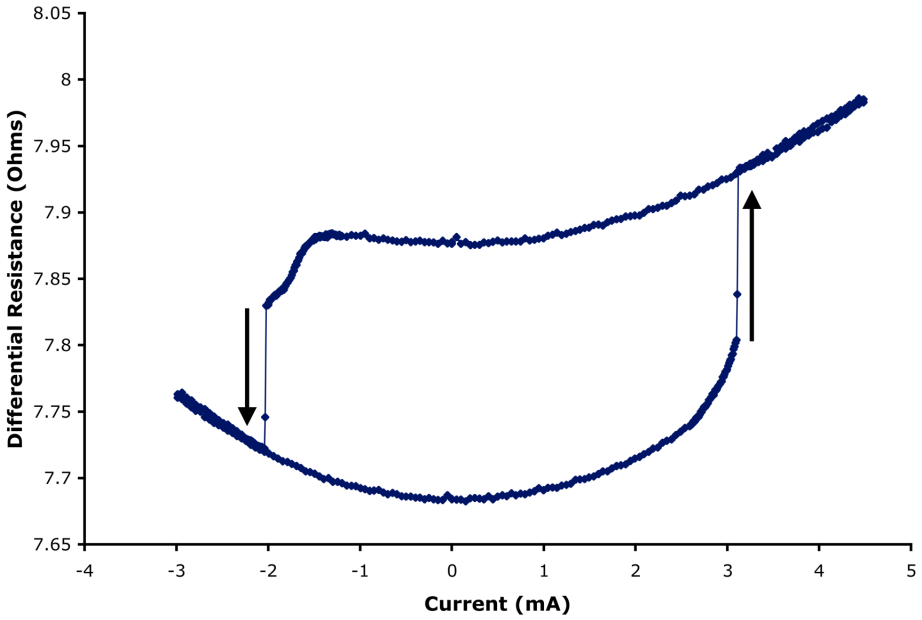

Figure 4.12: A Tb-doped sample at 150 K. The parabolic curvature is caused by Joule heating. Deviations caused by the onset of dynamics are also visible.

and then we can simply integrate to find

$$R(I) = \frac{V}{I} = \frac{A}{3}I^2 + \frac{B}{2}I + C \tag{4.5}$$

which we can evaluate at I_c and compare to the $R(T)$ curve from the offset resistance of the Wheatstone bridge (see Figure 4.11).

Once we have corrected the device temperature for Joule heating and the switching currents for thermal promotion, we can finally plot the data and compare to the expected $1/T$ dependence for α. This is shown in Figure 4.13, where we find good agreement. This agreement in turn confirms that the spin-transfer critical currents are proportional to the damping parameter, and thus have the same temperature dependence.

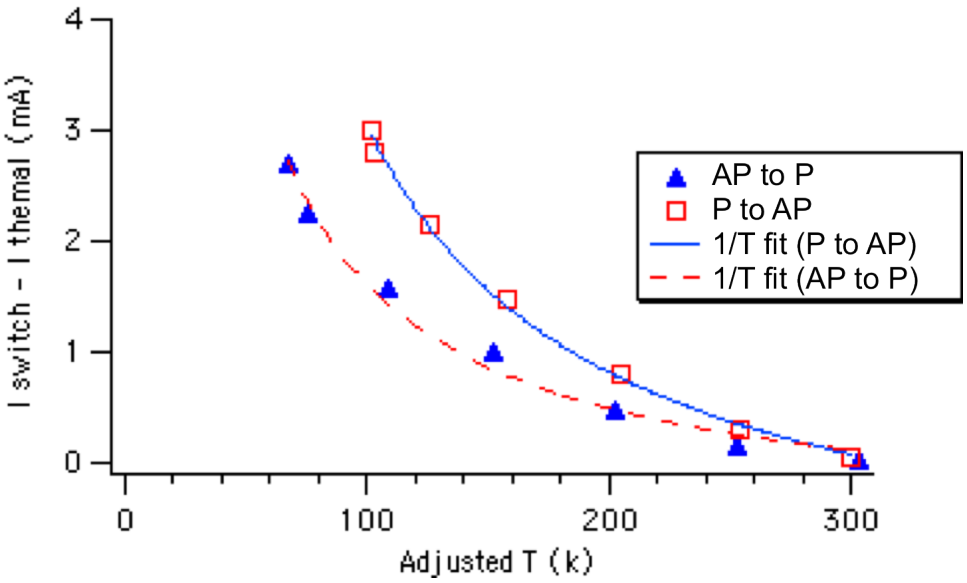

Figure 4.13: When the temperature is corrected for the Joule heating, and the critical current is corrected for thermal excitation over the barrier, then the temperature dependence of the critical current fits the $1/T$ expected from theory.

CHAPTER 5

APPLICATION RELEVANT RESULTS

5.1 Microwave Noise

A more practical concern for industrial applications than the temperature dependence is how the microwave noise generated by spin-transfer is affected. Recall that in addition to switching between stable states, the spin-transfer torque can also cause high frequency (GHz) oscillations, and that this noise is the primary deleterious effect for hard drive read heads. [45] [46] [47] To see if terbium doping can ameliorate this potential problem, we have measured the microwave noise in Py and PyTb samples.

Figure 5.1 sketches the detection set-up. The DC current is introduced to the sample through a bias-T, connected to the sample with a high-frequency probe. The resulting microwave signal travels up these same wires, but is directed by the bias-T toward the capacitive path. Here the signal travels through many stages of high frequency amplification, along with one 10 dB attenuator, before reaching the mixer. The attenuator is introduced to disrupt standing waves, and unlike the amplifiers, is bidirectional. The mixer combines the amplified signal with the output of the sweeper, modulating the signal. A low-pass (100MHz) filter removes all of the components of the signal that did not match the sweeper's frequency, in a manner that closely resembles the workings of a conventional lock-in amplifier. The diode converts the microwave power into a DC voltage that is recorded, along with the mixing frequency.

Figure 5.2 shows the noise power across many different fields. The fields

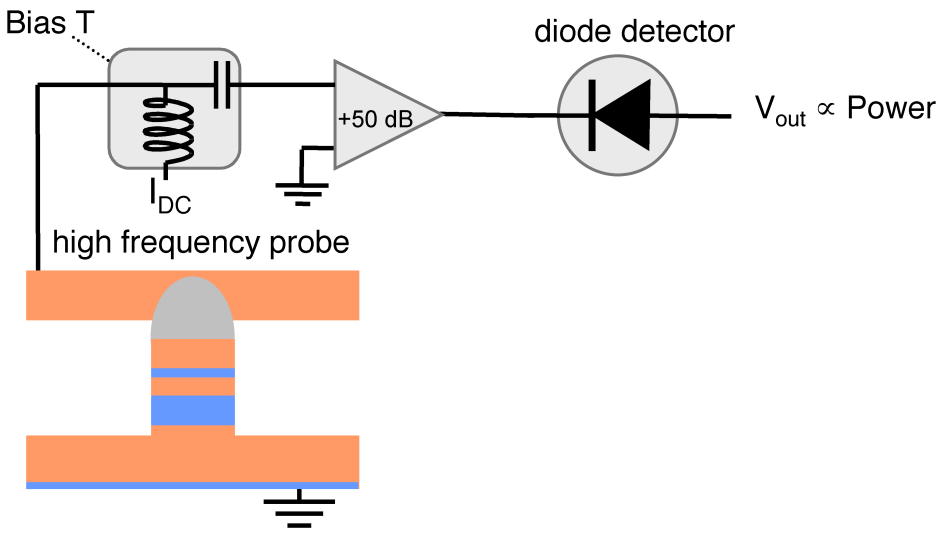

Figure 5.1: Sketch of the DC dynamics detection set-up

between zero and the lowest field shown are not mentioned in the legend because, as at zero field, they show no signal. The applied field contributes to the balance between damping and spin torque necessary for stable precession. With high enough current the sample will switch instead of stably precessing, as seen at the lower fields. The control sample has to be zoomed in just to be on the same scale as the terbium sample. In this comparison, it is clear that the onset current for microwave noise is also greatly enhanced by the terbium doping.

Because of standing waves, partial reflections, and other frequency-dependent phenomena, the gain of the amplification system must be calibrated at each frequency. This is done using a resistor in the place of the sample. The Johnson noise is measured at room temperature (300 K) and then again with the resistor submersed in liquid nitrogen (77 K). Because the temperature dependence of the Johnson noise of a resistor is known, the difference between these measurements tells us the frequency-dependent gain of the system.

Using this calibration and summing over all frequencies measured, we

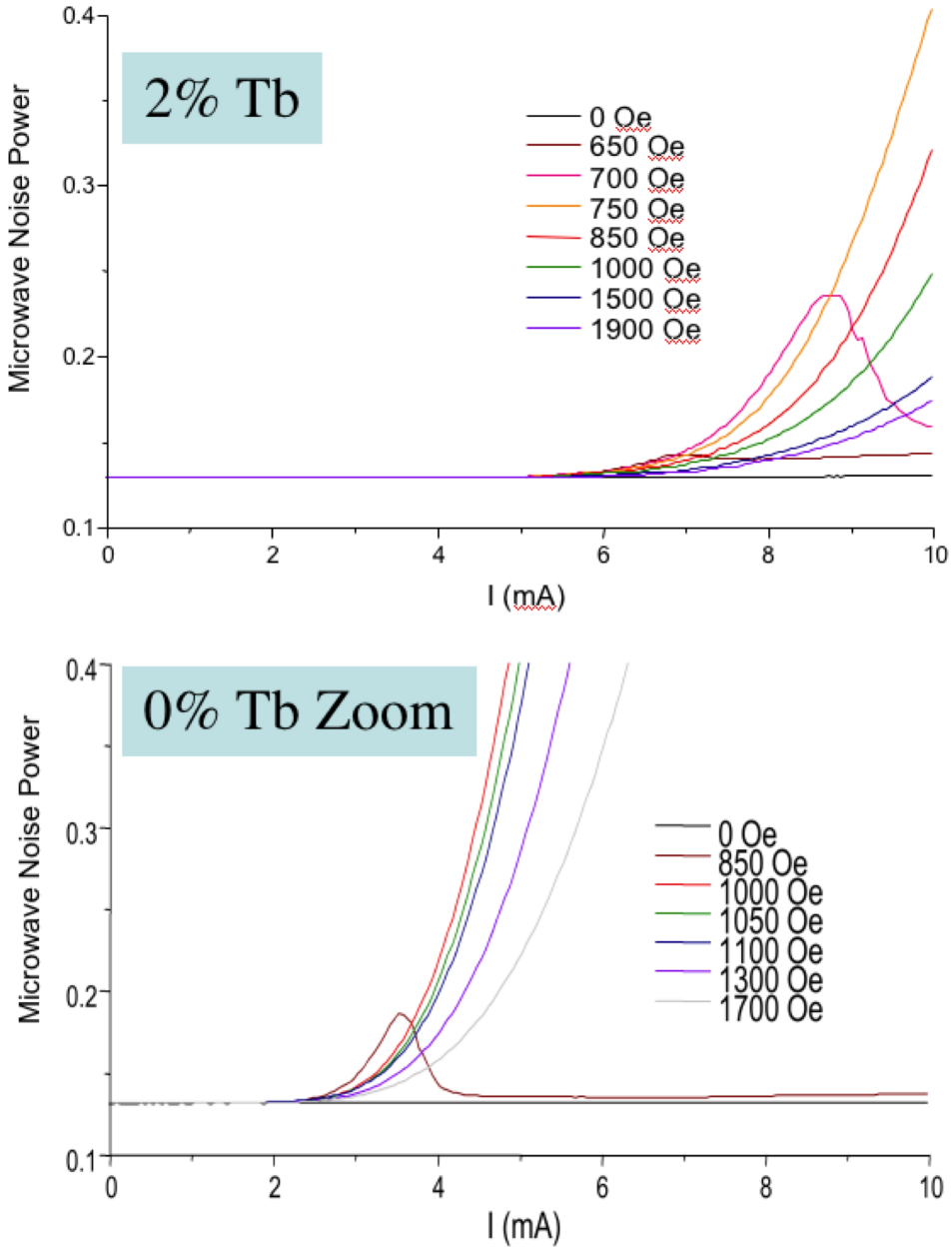

Figure 5.2: In the terbium sample, the sample requires much more current to excite microwave noise.

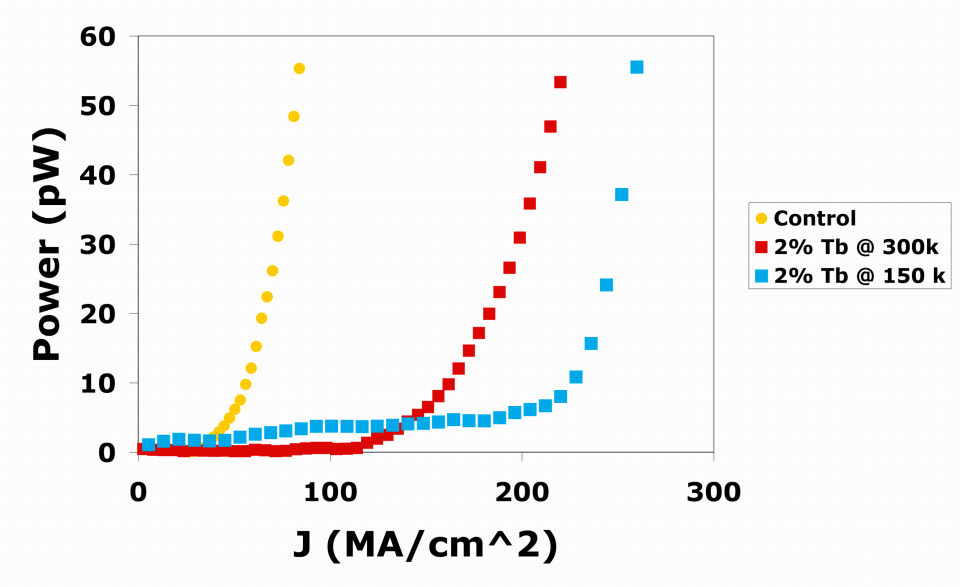

Figure 5.3: The Tb doped samples require higher currents to produce significant microwave noise. The 150 K data has drifting contact resistance, and would otherwise show no power below 200 MA/cm^2

achieve the plot shown in Figure 5.3. Again, the terbium-doped sample has a higher threshold for microwave noise than the undoped Py control sample. As with the DC switching measurements, this effect is more pronounced at lower temperatures.

5.2 High-Speed Pulse Measurements

Two possible concerns regarding the use of Tb dopants in hard drive read heads are immediately apparent: the Tb may decrease the ΔR signal and it may lengthen the switching time. The reduction of $\Delta R/R$ with the addition of Tb to the system is still a legitimate concern, but our samples do not show a large effect. The difference in ΔRA between the Tb doped samples and the control

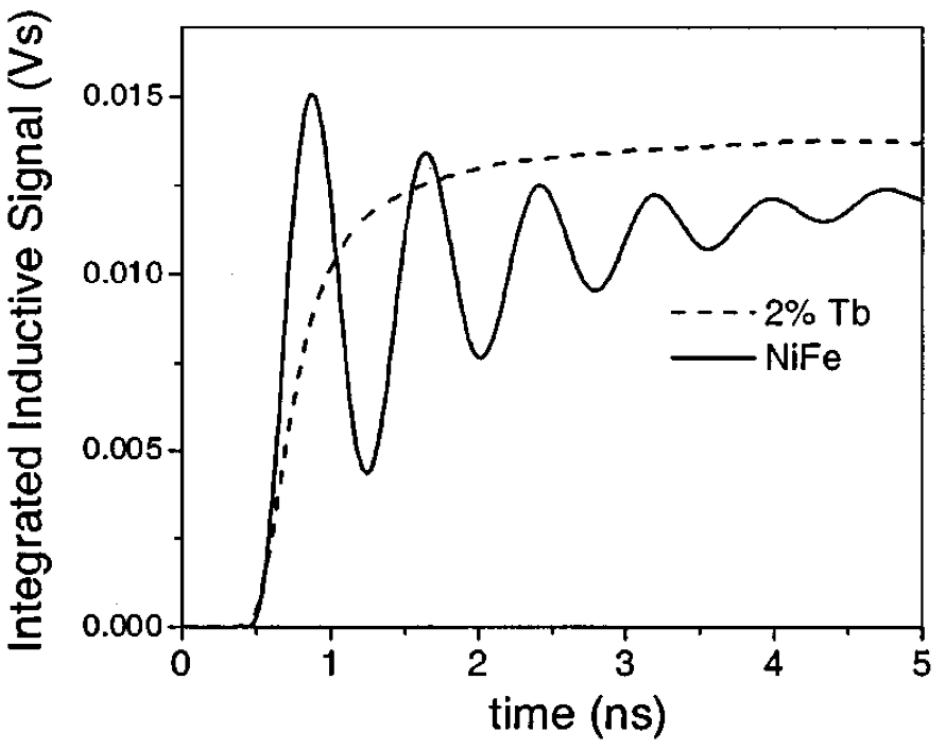

Figure 5.4: NIST measurement of the inductive response of continuous 50 nm Py films to a 60 ps rise-time magnetic field pulse. The pure Py sample is underdamped, while the Tb-doped sample reaches equalibrium quicker. From Russek.[48]

samples, while measurable, is within the 15 percent variation arising from uncertainty in area measurement and fabrication variation. As the seminal work at NIST [32] shows, pure permalloy is underdamped, leading to a ringing phenomenon, as seen in Figure 5.4. Raising the damping with Tb doping should bring the system closer to critical damping and minimal switching time. Still, the DC switching measurements are at a slow time scale compared to the hard drive read heads that will be the application of this work. We can investigate the performance of Tb samples in a high speed regime by switching them with nanosecond pulses.

The workings of the pulsed experiment are simple. Instead of a continuous

current slowly increased until switching takes place, a short pulse of current is applied with the pulse length in the same nanosecond regime in which magnetodynamics takes place. Over a second later, the resistance to the device is measured using the same method used in the DC measurements to determine if switching took place. If the device is measured as switched, then the DC reset current is ramped up past the switching value in the other direction to restore the starting condition, then back down to zero for another measurement after confirming that it has switched back. Since the pulses may not be long enough for the system to reach equilibration, and because of random variation in the starting condition, a large number of pulse switching attempts (between 100 and 500) were made to accurately determine the switching probability as a function of field, current, and pulse length. The resulting curves are fit to macrospin simulations to infer otherwise difficult to measure microscopic parameters such as effective damping and spin torque efficiency.

A complication arises because the pulse generators are not able to produce pulses of arbitrary magnitude, but only those that are an integer number of decibels smaller than the maximum amplitude pulse. Depending on the sample resistance, that can cause the current steps to be widely spaced, giving poor resolution. This discretization creates the possibility, realized in many devices, of jumping from 0 % to 100 % with few or no data points in between. To address this issue, we add a DC offset current that offers microamp precision. As long as the DC current is much smaller than the switching current, then the free layer will remain in its equilibrium position until the pulse is applied, and the results will match the ideal case of a continuous amplitude pulse generator. This correspondence allows us to treat the pulse and offset combination as if it is simply a larger pulse.

Indeed, this offset technique is useful as a the calibration method for the current pulses. We simply determine the amount of DC offset current necessary to compensate for 1 dB of attenuation, and then solve for the magnitude of the current pulses. We make this determination by measuring the switching probability of the chosen sample in response to pulses without any DC offset, then choose the attenuation value that gives a probability closest to 50%, to be near the steep portion of the curve. Then we simply increase the amount of DC offset current applied to pulses with 1 dB more attenuation until we reach the same percentage of switching measured initially. We note in passing that this technique relies on the monotonic nature of switching probability in response to current. Since any errors in the calibration will be systematic errors, we take a factor of 10 more samples during the calibration phase, to minimize statistical noise. This calibration strategy allows us to avoid the potential inaccuracies introduced by using a voltage source for the pulse, and sample variations such as contact resistance.

The curve relating switching probability to the amplitude of the current pulse is then compared to a similar curve generated by simulation[42], thus fitting for the damping and spin torque efficiency. Unfortunately, even for the control samples, the damping values generated are inconsistent with other methods[49], probably due to a breakdown at large angles in the macrospin approximation that the simulations rely upon. For the Tb samples, with their high critical currents that create larger Oersted fields (one of the causes of the magnetic inhomogeneities that can violate the macrospin approximation) and heating effects, the inconsistencies should be expected to be larger, and indeed extend to within a sample. Better, more direct measurements of α will be addressed in Section 5.3.

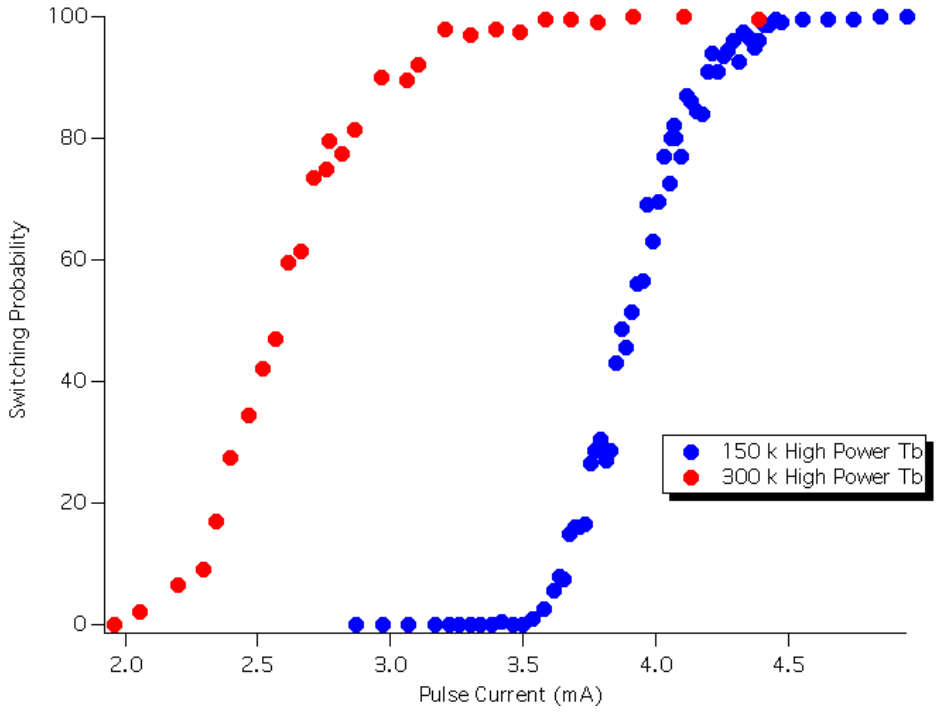

Figure 5.5: Switching probablity vs. pulse amplitude for a 1 nsec pulse length at room and low temperature.

From an application standpoint, the data are sufficient to decide the suitability of teribum-doped devices for use at the high speeds modern hard drives demand. Figure 5.5 shows results for the Tb samples with 1 nsec pulses. We again see that higher damping at lower temperature requires more current to switch. But even in the higher damping regime reached at the lower temperature, the devices still switch reliably for a sufficiently large pulse. Concerns that the higher damping would prevent the devices from switching quickly enough to meet industry demands at reasonable currents prove to be unfounded.

5.3 Measuring Alpha in Py and CoFe

Given the large role the Gilbert phenomenological damping parameter has in our research, it is natural that we attempt to measure α directly. Unfortunately, we lacked that experimental capability at the time our samples were made, so we could not characterize or optimize the films before creating the nanopillars. We could only return later and try other techniques to measure the original wafers that were optimized for nanofabrication. Towards this end, we pursued measuring the inductive response to pulsed field in collaboration with NIST[32], fitting to the pulsed switching data, and fitting to in-plane[49] Spin Torque FMR[50] [51], but without satisfactory results. In particular, the combination of a layer made thin enough for spin-transfer along with greatly increased damping created tremendous complications for efforts to achieve sufficient signal to make a precise measurement. The presence of the fixed layer only made matters worse. Fortunately, we now have the capability to make FMR measurements on thin films directly, from which the damping can be deduced.

The samples, sputtered expressly for FMR measurements once they were possible, are extended thin films with 30 nm of magnetic material, capped with 5 nm of Cu and 5 nm of Pt, to prevent oxidation. One sample, instead of being spatially uniform like the others, consisted of 15 nm of 4% Tb surrounded by two 7.5 nm layers of pure Py, to create an effectively 2% Tb sandwich. The FMR measurements[52] [53] were done using a Flip-Chip method with a gold coplanar waveguide and a network analyzer[54] [55] on extended thin films that were sputtered for this purpose. While we did not recalibrate the co-sputtering with XPS as we did for the spin-transfer samples, we used the same conditions as before for the PyTb alloy. Since the deposition rates of Py and CoFe are within

Magnetic Layer	Nominal Tb %	Alpha
Pure Py	0	0.0074
Pure Py	2%	0.046
Py Sandwich	2%	0.043
Pure Py	4%	0.078
CoFe	0	0.0078
CoFe	2%	0.09

Table 5.1: FMR Measurements

10% of each other, we expect the terbium concentration to be the same (2%) to that level of accuracy. Still, the CoFe numbers especially should be considered estimates. The results are shown in Table 5.1. The fact that the sandwich has the same damping as the pure 2% Tb suggests that our approximation of treating the Tb as isolated ions is a good one. If Tb-Tb interactions play a significant role, we would expect to see a non-linear effect on the damping when we change the Tb density.

The CoFeTb measurements were motived by earlier measurements of extended thin films at low temperatures, shown in Figure 5.6. The in-plane coercive field was measured with a SQUID. At low temperatures the terbium clearly increases the anisotropy [56], in both the Py and CoFe samples. This similarity of interaction in an effect that also involves spin-orbit coupling[56] suggested that we explore the damping in the CoFe system as well.

We speculate that the increased α in the CoFe sample (greater than the increase in the Py sample) is due to the larger iron faction, on the expectation that Fe-Tb interactions dominate. It could also be that Co acts more like Fe than Ni in this case, with the larger M_s promoting the interaction. It would be interesting to explore how these terbium-induced effects are affected by the relative concentrations of Ni, Fe, and Co, but that will have to wait for further work.

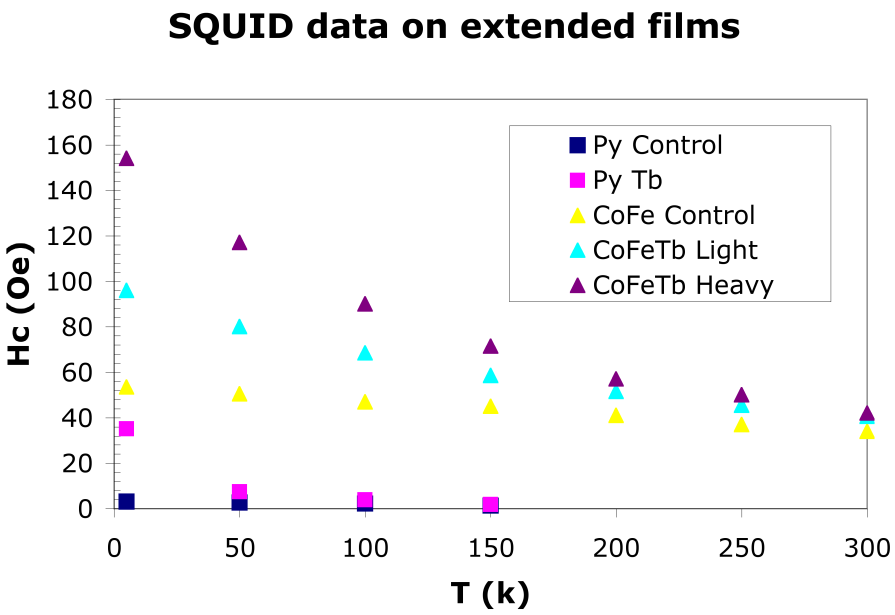

Figure 5.6: The effect of Terbium on coercive field for Py and CoFe.

CHAPTER 6

SUMMARY

In summary, we have fabricated spin-transfer nanopillars and dramatically enhanced their damping with terbium doping. We see this damping enhancement reflected in much larger critical currents required for spin-transfer switching, in sharp contrast to the undoped control samples. This effect is much stronger at lower temperatures, which we can understand through the application of theory from the iron garnets. Good agreement was found between the 1/T temperature dependence predicted therein and the switching data, but only after carefully accounting for the premature switching through thermal promotion with a Kurkijarvi-like theory and the effective temperature from the Joule heating caused by the very large currents required to switch such heavily damped devices.

We have also shown that terbium doping can address technological issues with hard drive read heads. In particular, it can suppress the microwave noise to a higher threshold current without compromising the ability to switch the device in 1 nsec at a reasonable pulsed current amplitude. Finally, we made direct FMR measurements of the Gilbert phenomenological damping parameter and found cause to suggest CoFe as a system for potential follow-up work.

BIBLIOGRAPHY

[1] N. C. Emley, F. J. Albert, E. M. Ryan, I. N. Krivorotov, D. C. Ralph, R. A. Buhrman, J. M. Daughton, and A. Jander. *Applied Physics Letters*, **84**, 4257 (2004).

[2] M.D. Stiles and A. Zangwill. *Physcial Review B*, **66**, 014407 (2002).

[3] M.D. Stiles. *Journal of Applied Physics*, **79**, 5805 (1996).

[4] C. Chappert, A. Fert, and F. Nguyen Van Dau. *Nature Materials*, **6**, 813 (2007).

[5] G. Binasch, P. Griinberg, F. Saurenbach, and W. Zinn. *Physical Review B*, **39**, 4828 (1989).

[6] M. N. Baibich, J. M. Broto, A. Fert, F. Nguyen Van Dau, F. Petroff, P. Etienne, G. Creuzet, A. Friedrich, and J. Chazelas. *Physical Review Letters*, **61**, 2472 (1988).

[7] W. P. Pratt Jr., S.-F. Lee, J. M. Slaughter, R. Loloee, P. A. Schroeder, and J. Bass. *Physical Review Letters*, **66**, 3060 (1991).

[8] I. N. Krivorotov, N. C. Emley, A. G. F. Garcia, J. C. Sankey, S. I. Kiselev, D. C. Ralph, and R. A. Buhrman. *Physical Review Letters*, **93**, 166603 (2004).

[9] M. Tsoi, A. G. M. Jansen, J. Bass, W. C. Chiang, M. Seck, V. Tsoi, and P. Wyder. *Physical Review Letters*, **80**, 4281 (1998).

[10] E. B. Myers, D. C. Ralph, J. A. Katine, R. N. Louie, and R. A. Buhrman. *Science*, **285**, 867 (1999).

[11] J. A. Katine, F. J. Albert, R. A. Buhrman, E. B. Myers, and D. C. Ralph. *Physical Review Letters*, **84**, 3149 (2000).

[12] S. I. Kiselev, I. N. Krivorotov J. C. Sankey and, N. C. Emley, R. J. Schoelkopf, R. A. Buhrman, and D. C. Ralph. *Nature*, **425**, 380 (2003).

[13] T.L. Gilbert. *Physical Review*, **100**, 1243 (1955).

[14] L. Landau and E. Lifshitz. *Phys. Zeitsch. der Sowjetunion*, **8**, 153–169 (1953).

[15] J. C. Slonczewski. *Journal of Magnetism and Magnetic Materials*, **159**, L1 (1996).

[16] L. Berger. *Physical Review B*, **54**, 9353 (1996).

[17] J. Z. Sun. *Physical Review B*, **62**, 570 (2000).

[18] D.C. Ralph and M.D. Stiles. *Journal of Magnetism and Magnetic Materials*, **320**, 1190 (2008).

[19] S. Ingvarsson, L. Ritchie, X. Y. Liu, Gang Xiao, J. C. Slonczewski, P. L. Trouilloud, and R. H. Koch. *Physical Review B*, **66**, 214416 (2002).

[20] V. Kambersky. *Canadian Journal of Physics*, **48**, 2906 (1970).

[21] J. Kunes and V. Kambersky. *Physical Review B*, **65**, 212411 (2002).

[22] V. Kambersky. *Czechoslovak Journal of Physics*, **26**, 1366 (1976).

[23] V. Korenman. *Physical Review B*, **9**, 3147 (1974).

[24] V. Korenman and R. E. Prange. *Physical Review B*, **6**, 2769 (1972).

[25] L. Berger. *Journal of Physics and Chemistry of Solids*, **38**, 1321 (1977).

[26] B. Heinrich, D. Fraitov, and V. Kambersky. *Physica Status Solidi (B)*, **23**, 501 (1967).

[27] A. H. Mitchell. *Physical Review*, **105**, 1439 (1957).

[28] C. Kittel and A. H. Mitchell. *Physical Review*, **101**, 1611 (1956).

[29] K. Gilmore, Y. U. Idzerda, and M. D. Stiles. *Journal of Applied Physics*, **103**, 07D303 (2008).

[30] R. D. McMichael and D. J. Twisselmann. *Physical Review Letters*, **90**, 227601 (2003).

[31] Yaroslav Tserkovnyak, Arne Brataas, and Gerrit E. W. Bauer. *Physical Review B*, **66**, 224403 (2002).

[32] W. Bailey, P. Kabos, F. Mancoff, and Stephen Russek. *IEEE Transactions on Magnetism*, **37**, 1749 (2001).

[33] C. Kittel. *Physical Review*, **115**, 1587 (1959).

[34] P.G. De Gennes, C. Kittel, and A. M. Portis. *Physical Review*, **116**, 323 (1959).

[35] R. Pauthenet. *Ann. Phys. (Paris)*, **3**, 424 (1958).

[36] C. Kittel. *Elementary Satistical Physics*. John Wiley and Sons Inc., 1958.

[37] P. E. Seiden. *Physical Review*, **133**, A728 (1964).

[38] J. F. Dillon jr. *Physical Review*, **127**, 1495 (1962).

[39] Gerald F. Dionne and George L. Fitch. *Journal of Applied Physics*, **87**, 4963 (2000).

[40] M. D. Stiles and J. Miltat. *Spin Dynamics in Confined Magnetic Structures III: Topics in Applied Physics 101*, pages 225 – 308. Springer, 2006.

[41] O. Ozatay, P. G. Gowtham, K. W. Tan, J. C. Read, K. A. Mkhoyan, M. G. Thomas, G. D. Fuchs, P. M. Braganca, E. M. Ryan, K. V. Thadani, J. Silcox, D. C. Ralph, and R. A. Buhrman. *Nature Materials*, **7**, 567 (2008).

[42] P. M. Braganca, I. N. Krivorotov, O. Ozatay, A. G. F. Garcia, N. C. Emley, J. C. Sankey, D. C. Ralph, and R. A. Buhrman. *Applied Physics Letters*, **87**, 112507 (2005).

[43] E. B. Myers, F. J. Albert, J. C. Sankey, E. Bonet, R. A. Buhrman, and D. C. Ralph. *Physical Review Letters*, **89**, 196801 (2002).

[44] J. Kurkijarvi. *Physical Review B*, **6**, 832 (1972).

[45] M. Covington, M. AlHajDarwish, Y. Ding, N. J. Gokemeijer, and M. A. Seigler. *Physical Review B*, **69**, 184406 (2004).

[46] Alina Deac, Yue Liu, Olivier Redon, Sebastien Petit, Min Li, PoKang Wang, Jean-Pierre Nozires, and Bernard Dieny. *Journal of Physics: Condensed Matter*, **19**, 165208 (2007).

[47] R. Sbiaa and S. N. Piramanayagam. *Journal of Applied Physics*, **101**, 073911 (2007).

[48] Stephen E. Russek, Pavel Kabos, R. D. McMichael, C. G. Lee, William E. Bailey, Ricky Ewasko, and Steven C. Sanders. *Journal of Applied Physics*, **91**, 8659 (2002).

[49] G. D. Fuchs, J. C. Sankey, V. S. Pribiag, L. Qian, P. M. Braganca, A. G. F. Garcia, E. M. Ryan, Zhi-Pan Li, O. Ozatay, D. C. Ralph, and R. A. Buhrman. *Applied Physics Letters*, **91**, 062507 (2007).

[50] A. A. Talapurkar, Y. Suzuki, A. Fukushima, H. Kubota, H. Maehara, K. Tsunekawa, D. D. Kjayaprawira, N. Watanabe, and S. Yuasa. *Nature*, **438**, 339 (2005).

[51] J. C. Sankey, P. M. Braganca, A. G. F. Garcia, I. N. Krivorotov, R. A. Buhrman, and D. C. Ralph. *Physical Review Letters*, **96**, 227601 (2006).

[52] T. J. Klemmer, K. A. Ellis, and B. van Dover. *Journal of Applied Physics*, **87**, 5846 (2000).

[53] V. Korenivski, R. B. van Dover, P. M. Mankiewich, Z.-X. Ma, A. J. Becker, P. A.Polakos, and V. J. Fratello. *IEEE Transactions on Magnetics*, **32**, 4905 (1996).

[54] Sangita S. Kalarickal, Pavol Krivosik, Mingzhong Wu, Carl E. Patton, Michael L. Schneider, Pavel Kabos, T. J. Silva, and John P. Nibarger. *Journal of Applied Physics*, **99**, 093909 (2006).

[55] J-M. L. Beaujour, J. H. Lee, A. D. Kent, K. Krycka, and C-C. Kao. *Physical Review B*, **74**, 214405 (2006).

[56] Robert C. O'Handley. *Modern Magnetic Materials*. John Wiley and Sons Inc., 2000.